Journal of Fluids and Structures (2000) **14,** 635–668
doi:10.1006/jfls.2000.0289 available online at http://www.idealibrary.com on IDEAL®

A THEORETICAL MODEL FOR NONLINEAR ORBITAL MOTIONS OF ROTORS UNDER FLUID CONFINEMENT

M. Moreira and J. Antunes

Instituto Tecnológico e Nuclear, Applied Dynamics Laboratory ITN/ADL
2686 Sacavém Codex, Portugal

and

H. Pina

Instituto Superior Técnico, Mechanical Engineering Department IST/DEM
Av. Rovisco Pais, 1096 Lisboa Codex, Portugal

(Received 5 July 1999, and in final form 1 February 2000)

In previous papers, Antunes and co-workers developed a theoretical model for nonlinear *planar* motions—motions $X(t)$ taking place in one single direction—of rotors under fluid confinement using simplified flow equations on the gap-averaged fluctuating quantities. The nonlinear solution obtained was shown to be consistent with a linearized solution for the same problem. Also, it displayed an encouraging qualitative agreement between the nonlinear theory and preliminary experimental results. Following a similar approach, the nonlinear theoretical model is here extended to cope with *orbital* rotor motions—motions $X(t)$ and $Y(t)$ taking place in two different orthogonal directions—by developing an exact formulation for the two-dimensional dynamic flow forces. Numerical simulations of the nonlinear rotor–flow coupled system are presented and compared with the linearized model. These yield similar results when the eccentricity and the spinning velocity are low. However, if such conditions are not met, the qualitative dynamics stemming from the linearized and nonlinear models may be quite distinct. Preliminary experimental results also indicate that the nonlinear flow model leads to better predictions of the rotor dynamics when the eccentricity is significant, when approaching instability, and for linearly unstable regimes.

1. INTRODUCTION

Vibration of rotating shafts subjected to fluid–structure interaction is a physical problem of both theoretical significance and practical importance, as convincingly demonstrated in many references [see, for instance, books by Vance (1988) and Goodwin (1989)]. This problem has been studied for different gap geometries, ranging from bearing configurations to pump systems. Here we are interested in the rotor dynamics under moderate fluid confinement (with reduced gap $\delta = H/R$ of about 0·1, where H is the annular fluid gap and R is the rotor radius).

Rotor dynamics under moderate fluid confinement have been studied since Black (1969), Fritz (1970) and Hirs (1973). Further relevant work was presented by several authors including Ramsden *et al.* (1974, 1975), Childs (1983), Nelson (1985) and Nordmann *et al.* (1989). A thorough analysis using linearized flow equations on the gap-averaged fluctuating quantities was performed by Grunenwald *et al.* (1991), Axisa & Antunes (1992), Grunenwald (1994) and Antunes *et al.* (1996).

0889–9746/00/070635 + 34 $35.00/0

Recently, a theoretical formulation for the fully nonlinear *planar* motions showed an encouragingly better agreement with experimental results (Antunes *et al.* 1999). The same assumptions and methods will be used to develop a theoretical model for nonlinear *orbital* motions of rotors. The difficult integrations which arise were conveniently solved here by using basic complex analysis techniques.

2. FLOW FORMULATION

Consider the geometry of the fluid annulus represented in Figure 1, where θ and t are, respectively, the azimuthal angle and time, R is the shaft radius and $u(\theta, t)$ is the gap-averaged tangential flow velocity. The annular gap depth $h(\theta, t)$ is very well approximated by

$$h(\theta, t) = H - X(t)\cos\theta - Y(t)\sin\theta, \tag{1}$$

where H is the average annular gap.

The following simplifying assumptions will be adopted concerning the flow field [see Antunes *et al.* (1997)]: (i) the flow is modelled as being two-dimensional and incompressible; (ii) the radial gradients in the velocity and pressure fields are neglected; (iii) the dissipative effects due to turbulent shear stresses at the walls are modelled using semiempirical loss-of-head terms.

With these assumptions, one can obtain the continuity equation for incompressible flow and the momentum equation (projected in the tangential direction),

$$\frac{\partial h}{\partial t} + \frac{1}{R}\frac{\partial (hu)}{\partial \theta} = 0, \tag{2}$$

$$\rho\left\{\frac{\partial (hu)}{\partial t} + \frac{1}{R}\frac{\partial (hu^2)}{\partial \theta}\right\} + \tau_s + \tau_r + \frac{h}{R}\frac{\partial p}{\partial \theta} = 0, \tag{3}$$

where ρ is the fluid density and $p(\theta, t)$ is the gap-averaged pressure.

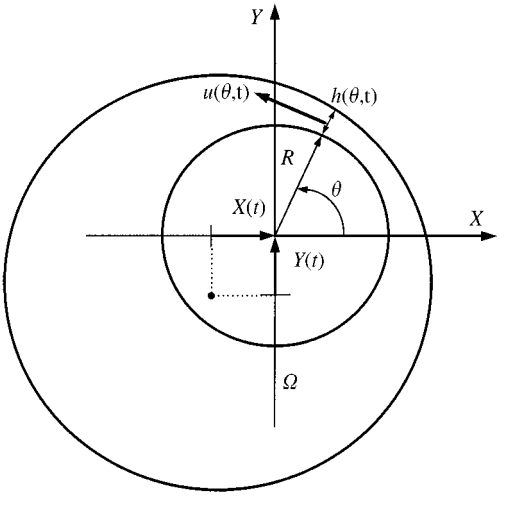

Figure 1. Geometry of the fluid annulus.

The shear stresses at the rotor and stator walls, in equation (3), are given by

$$\tau_s(\theta, t) = \frac{1}{2}\rho u|u| f_s,$$
$$\tau_r(\theta, t) = -\frac{1}{2}\rho(\Omega R - u)|\Omega R - u| f_r, \tag{4}$$

where f_r and f_s are empirical friction coefficients, which depend on the flow Reynolds number and on the roughness of the walls.

Among several empirical correlations, those suggested by Wend (1933) and Hirs (1973) are formulated as

$$f = a(\mathrm{Re})^b, \tag{5}$$

where coefficients a and b are obtained from experiments. As given above, the shear stresses change in a quadratic way with the flow velocity and always oppose the flow—hence the moduli in equations (4).

Assuming $f_r = f_s = f$, we can deduce

$$\tau_s + \tau_r = \begin{cases} -\rho f u^2 + \rho f \Omega R u - \frac{1}{2}\rho f \Omega^2 R^2 & \text{if } u \leq 0, \\ +\rho f \Omega R u - \frac{1}{2}\rho f \Omega^2 R^2 & \text{if } 0 < u \leq \Omega R, \\ +\rho f u^2 - \rho f \Omega R u + \frac{1}{2}\rho f \Omega^2 R^2 & \text{if } u > \Omega R. \end{cases} \tag{6}$$

This simplification is adequate except in quite extreme conditions, such as when the roughnesses of the rotor and the stator walls are quite different (Grunenwald *et al.* 1996). One can observe the corresponding normalized skin-friction stresses as a function of the reduced flow velocity in Figure 2.

In the following, we will be interested in the dynamic flow forces

$$F_X(t) = -LR\int_0^{2\pi} p(\theta, t)\cos\theta\, \mathrm{d}\theta,$$
$$F_Y(t) = -LR\int_0^{2\pi} p(\theta, t)\sin\theta\, \mathrm{d}\theta, \tag{7}$$

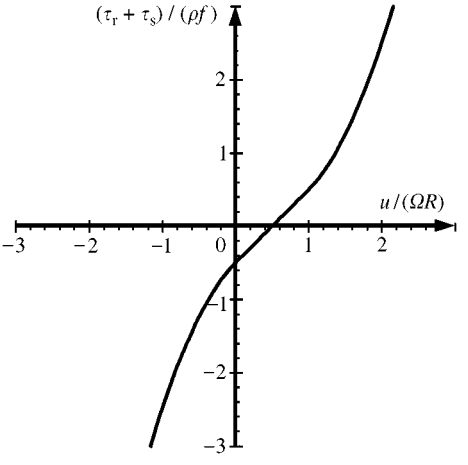

Figure 2. Skin-friction stresses as a function of the reduced flow velocity (with $f_r = f_s = f$).

where L is the immersed length of the rotor. Equivalently, by integration by parts, one can express equations (7) in a more convenient way as

$$F_X(t) = LR\int_0^{2\pi} \frac{\partial p(\theta,t)}{\partial\theta}\sin\theta\,\mathrm{d}\theta,$$
$$F_Y(t) = -LR\int_0^{2\pi} \frac{\partial p(\theta,t)}{\partial\theta}\cos\theta\,\mathrm{d}\theta. \tag{8}$$

3. SOLUTION OF THE FLOW EQUATIONS

From equation (2), the velocity field is obtained directly as

$$u(\theta,t) = \frac{R(\dot{X}(t)\sin\theta - \dot{Y}(t)\cos\theta + C(t))}{H - X(t)\cos\theta - Y(t)\sin\theta}, \tag{9}$$

where $C(t)$ is an integration constant, which can be shown to be proportional to the average bulk-flow velocity.

Considering the following forms of equation (3):

$$-\frac{\partial p}{\partial\theta}\sin\theta = \rho\left\{R\frac{\partial(hu)}{h\partial t} + \frac{\partial(hu^2)}{h\partial\theta}\right\}\sin\theta + R\frac{\tau_s+\tau_r}{h}\sin\theta, \tag{10}$$

$$-\frac{\partial p}{\partial\theta}\cos\theta = \rho\left\{R\frac{\partial(hu)}{h\partial t} + \frac{\partial(hu^2)}{h\partial\theta}\right\}\cos\theta + R\frac{\tau_s+\tau_r}{h}\cos\theta, \tag{11}$$

$$-\frac{1}{R}\frac{\partial p}{\partial\theta} = \rho\left\{\frac{\partial(hu)}{h\partial t} + \frac{1}{R}\frac{\partial(hu^2)}{h\partial\theta}\right\} + \frac{\tau_s+\tau_r}{h}, \tag{12}$$

and utilizing equations (6), (8) and (9), one can deduce

$$F_X(t) = -\rho R^2 L\mathbb{I}_1^X(t) - \rho RL\mathbb{I}_2^X(t) - R^2L\mathbb{I}_3^X(t), \tag{13}$$

$$F_Y(t) = \rho R^2 L\mathbb{I}_1^Y(t) + \rho RL\mathbb{I}_2^Y(t) + R^2L\mathbb{I}_3^Y(t), \tag{14}$$

$$0 = \rho\mathbb{I}_1(t) + \frac{\rho}{R}\mathbb{I}_2(t) + \mathbb{I}_3(t), \tag{15}$$

where

$$\mathbb{I}_1^X(t) \equiv \int_0^{2\pi}\frac{\partial(hu)}{h\partial t}\sin\theta\,\mathrm{d}\theta, \quad \mathbb{I}_2^X(t) \equiv \int_0^{2\pi}\frac{\partial(hu^2)}{h\partial\theta}\sin\theta\,\mathrm{d}\theta, \tag{16, 17}$$

$$\mathbb{I}_3^X(t) \equiv \int_0^{2\pi}\frac{(\tau_s+\tau_r)}{h}\sin\theta\,\mathrm{d}\theta, \tag{18}$$

$$\mathbb{I}_1^Y(t) \equiv \int_0^{2\pi}\frac{\partial(hu)}{h\partial t}\cos\theta\,\mathrm{d}\theta, \quad \mathbb{I}_2^Y(t) \equiv \int_0^{2\pi}\frac{\partial(hu^2)}{h\partial\theta}\cos\theta\,\mathrm{d}\theta, \tag{19, 20}$$

$$\mathbb{I}_3^Y(t) \equiv \int_0^{2\pi}\frac{(\tau_s+\tau_r)}{h}\cos\theta\,\mathrm{d}\theta, \tag{21}$$

$$\mathbb{I}_1(t) \equiv \int_0^{2\pi}\frac{\partial(hu)}{h\partial t}\,\mathrm{d}\theta, \quad \mathbb{I}_2(t) \equiv \int_0^{2\pi}\frac{\partial(hu^2)}{h\partial\theta}\,\mathrm{d}\theta, \quad \mathbb{I}_3(t) \equiv \int_0^{2\pi}\frac{(\tau_s+\tau_r)}{h}\,\mathrm{d}\theta. \tag{22, 23, 24}$$

The integral factors $\mathbb{I}_3^X(t)$, $\mathbb{I}_3^Y(t)$ and $\mathbb{I}_3(t)$ were computed by using the linear branch of the plot $\tau_s + \tau_r$, as a function of $u(\theta, t)$, which is formulated in equation (6):

$$\tau_s + \tau_r \simeq \rho f \Omega R u - \tfrac{1}{2} \rho f \Omega^2 R^2. \tag{25}$$

Indeed, transitions between the branches of equation (6) cannot be decided *a priori*, as they depend on the spinning velocity Ω and rotor motion, from which stems the velocity field $u(\theta, t)$. This leads to a nonlinear model [equations (13) and (14)] which does not have a dissipative term when $\Omega = 0$. This problem has been discussed by Antunes *et al.* (1999).

All the previous integral factors are expanded in Appendix A. The expressions

$$G_k^{ij} = \int_0^{2\pi} \frac{\sin^i \theta \cos^j \theta}{(H - X\cos\theta - Y\sin\theta)^k} \, \mathrm{d}\theta, \tag{26}$$

referred to therein are presented in Appendix B. These integrals were computed as functions of the parameters H, $X(t)$ and $Y(t)$ using the residue theorem from complex analysis. This approach proved to be more effective than direct integration (in the real domain) used in the previous work (Antunes *et al.* 1999).

Letting $Y = \dot{Y} = \ddot{Y} = 0$, equations (13)–(15) collapse into

$$F_X(t) = \mathbb{D}_1 \ddot{X} + \mathbb{D}_2 \dot{X} + \mathbb{D}_3 \dot{X}^2 + \mathbb{D}_4 C^2, \tag{27}$$

$$0 = \dot{C} + \frac{X\dot{X} + RH\Omega f}{H^2 - X^2} C - \frac{1}{2} R\Omega^2 f, \tag{28}$$

where

$$\mathbb{D}_1 = -\pi\rho L R^3 \left[2 \frac{H - \sqrt{H^2 - X^2}}{X^2} \right], \quad \mathbb{D}_2 = -\pi\rho L R^3 \left[2R\Omega f \frac{H - \sqrt{H^2 - X^2}}{X^2 \sqrt{H^2 - X^2}} \right],$$

$$\mathbb{D}_3 = -\pi\rho L R^3 \left[\frac{\left(H - \sqrt{H^2 - X^2}\right)^2}{X^3 \sqrt{H^2 - X^2}} \right], \quad \mathbb{D}_4 = -\pi\rho L R^3 \left[-\frac{X}{(H^2 - X^2)^{3/2}} \right].$$

Equations (27) and (28) can be found in Antunes *et al.* (1999) and they describe a nonlinear *planar flow force*, F_X in a similar geometry. It was shown that F_X is an extension of the *linearized force for a centred* or *eccentric rotor*.

On the other hand, analysing the asymptotic behaviour of equations (13)–(15), when $\dot{X} = \ddot{X} = \dot{Y} = \ddot{Y} = 0$, one can obtain

$$|\bar{F}_{\bar{A}}| = \frac{\pi\rho L R^3 \Omega^2}{4} \frac{E}{H} \frac{\sqrt{H^2 - E^2}}{H},$$

$$|\bar{F}_{\bar{B}}| = \pi\rho L R^4 \Omega^2 f \frac{1}{HE} (H - \sqrt{H^2 - E^2}),$$

$$C = \frac{1}{2} \Omega \frac{H^2 - E^2}{H},$$

which are solutions of the steady flow we can find in Antunes *et al.* (1996). Note that $\bar{F}_{\bar{A}}$ and $\bar{F}_{\bar{B}}$ represent the steady flow forces, respectively, in directions $\bar{A} = X\mathbf{i} + Y\mathbf{j}$ and $\bar{B} = Y\mathbf{i} - X\mathbf{j}$.

From these arguments, the nonlinear flow equations (13)–(15), seem quite plausible. Note that a coupling between the rotor motions $X(t)$, $Y(t)$ and the auxiliary flow variable $C(t)$ is unavoidable when frictional effects are not neglected. Physically, equation (15) or equation

(28) can be related to delay effects of the flow responses to rotor motions, which depend on frictional phenomena. This issue will be addressed in detail elsewhere (Moreira *et al.* 2000)

4. ANALYSIS OF THE COUPLED SYSTEM

The motion equations of the rotor–flow coupled system read

$$M_{st}\,\ddot{X} + C_{st}\,\dot{X} + K_{st}X = F_X + F_X^{ext}, \tag{29}$$

$$M_{st}\,\ddot{Y} + C_{st}\,\dot{Y} + K_{st}Y = F_Y + F_Y^{ext}, \tag{30}$$

where $F_X^{ext}(t)$ and $F_Y^{ext}(t)$ stand for any external forcing functions and $F_X(t)$ and $F_Y(t)$ are given by the nonlinear fluidelastic forces (13) and (14), together with equation (15) which is necessary to close the problem. Equations (13)–(15), (29) and (30) can be expressed as

$$\ddot{X} = \mathbb{F}_1\,[\dot{X}, X, \dot{Y}, Y, C, F_X^{ext}, t], \tag{31}$$

$$\ddot{Y} = \mathbb{F}_2\,[\dot{X}, X, \dot{Y}, Y, C, F_Y^{ext}, t], \tag{32}$$

$$\dot{C} = \mathbb{F}_3\,[\ddot{X}, \dot{X}, X, \ddot{Y}, \dot{Y}, Y, C, F_X^{ext}, F_Y^{ext}, t], \tag{33}$$

or equivalently as a system of five nonlinear first-order coupled differential equations.

5. SIMULATION OF THE ORBITAL NONLINEAR MOTION

The five nonlinear first-order coupled differential equations were solved using an explicit algorithm of the Runge–Kutta type, with an error-controlled time-step based on the fourth- and fifth-order approximations (Press *et al.* 1992; Shampine 1994).

When the rotor eccentricity and the spinning velocity are low (e.g. the linear simplifying assumptions are fulfilled), the nonlinear numerical simulations yield similar results to those predicted by linear theory, while different kinds of instability phenomena arise only at eccentric configurations. In order to compare eccentric nonlinear numerical simulations with the Grunenwald *et al.* (1996) eccentric results, the specific static eccentricity (at 0 r.p.m.) of 60% was assumed.

So, the numerical simulations presented, are based on the significant eccentric configurations referred, which were labelled "*eccentric configuration* A" and "*eccentric configuration* B" in the experiments (using water) performed by Grunenwald *et al.* (1996). The significant parameters are shown in Table 1. Notice that Configuration B involves more than double the reduced gap δ compared with Configuration A.

TABLE 1

Parameters used for simulations

Eccentric configuration	A	B
L (rotor length, m)	0·250	0·250
R (rotor radius, m)	0·0470	0·0435
H (annular gap, m)	0·0032	0·0067
$\delta = H/R$ (reduced gap)	0·068	0·154
ε (static reduced eccentricity)	0·6	0·6
M_{st} (structural mass, kg)	6·9	7·0
C_{st} (structural damping, N s/m)	86	35
K_{st} (structural stiffness, N/m)	$1{\cdot}8 \times 10^4$	$1{\cdot}6 \times 10^4$
f_{st} [structural frequency $(1/2\pi)\sqrt{K_{st}/M_{st}}$ (Hz)]	8·1	7·6

The external excitation used in this simulation was a Gaussian random force, low-pass filtered outside the frequency range 0–30 Hz (of interest), of about 0.25 N r.m.s. Two different types of nonlinear simulations were performed, both of them with a maximum integration time-step much smaller than $1/(2 \times f_{\max})$, with $f_{\max} \approx 30$ Hz: (i) in the *first* type, the random excitation was applied, in both directions, in the initial 10 of the 15 s of total simulation, for each simulated spinning velocity; (ii) in the *second* type, the excitation was applied in only one direction and during 2 min, for each spinning velocity.

With the first set of simulations it was possible to perform the main identification tasks. Note that 10 s of Gaussian random force, applied with the time-step mentioned, is enough to excite periodic phenomena in the range from 0·1 to 30 Hz, with the corresponding resolution and obtain 5 s of free response after excitation to perform identification tasks.

The second set of tests were used to obtain statistically significant data to compute statistical tests such as histograms of response, values of kurtosis and skewness and finally, transfer/coherence function plots for each spinning velocity. Computation of transfer/coherence functions was performed using averaging techniques over the entire data set.

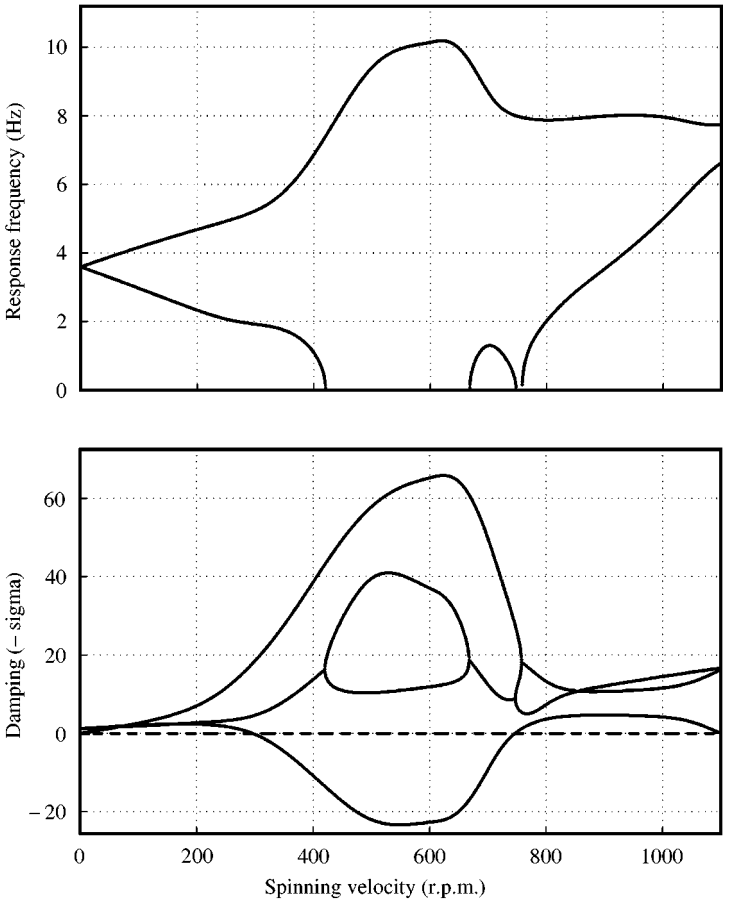

Figure 3. Configuration A: Rotor modes as a function of the spinning velocity; $\varepsilon = 0{\cdot}6$, $f = 0{\cdot}01$.

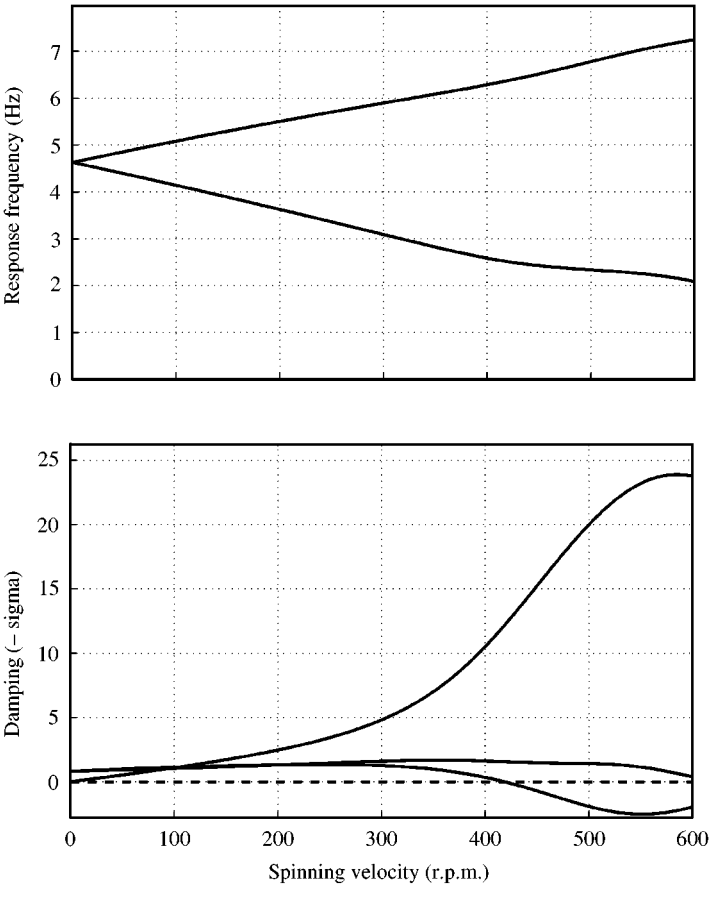

Figure 4. Configuration B: Rotor modes as a function of the spinning velocity; $\varepsilon = 0{\cdot}6$, $f = 0{\cdot}01$.

6. RESULTS AND DISCUSSION

6.1. Results Presented

In Figures 3 and 4 (Configuration A and Configuration B, respectively) one can observe the rotor model frequencies and damping values, as a function of the spinning velocity, predicted by an improved linear theory. These parameters stem from the five eigenvalues, $\lambda_n = \sigma_n + i\omega_n$ (one of them, always real), of the linearized equations (31)–(33). In addition to the forward and backward whirling modes predicted by our previous linearized model, there is now a zero-frequency mode related to the co-rotating flow. Because the improved linear model is rather involved, a separate paper will be presented on this topic shortly (Moreira *et al.* 2000).

Note that, because system dynamics are strongly dependent on the rotor eccentricity, the curves in Figures 3 and 4, were computed using an estimate of the *actual eccentricity* at each spinning velocity, which was obtained from nonlinear simulations. This explains the intricate behaviour of the computed eigenvalues, when compared with our previous studies.

In Figures 5 and 6 (Configuration A), and 16 and 17 (Configuration B), we present a comparison between the nonlinear numerical simulations, the linear theory and some published experiments (Grunenwald *et al.* 1991). These figures show the identified modal

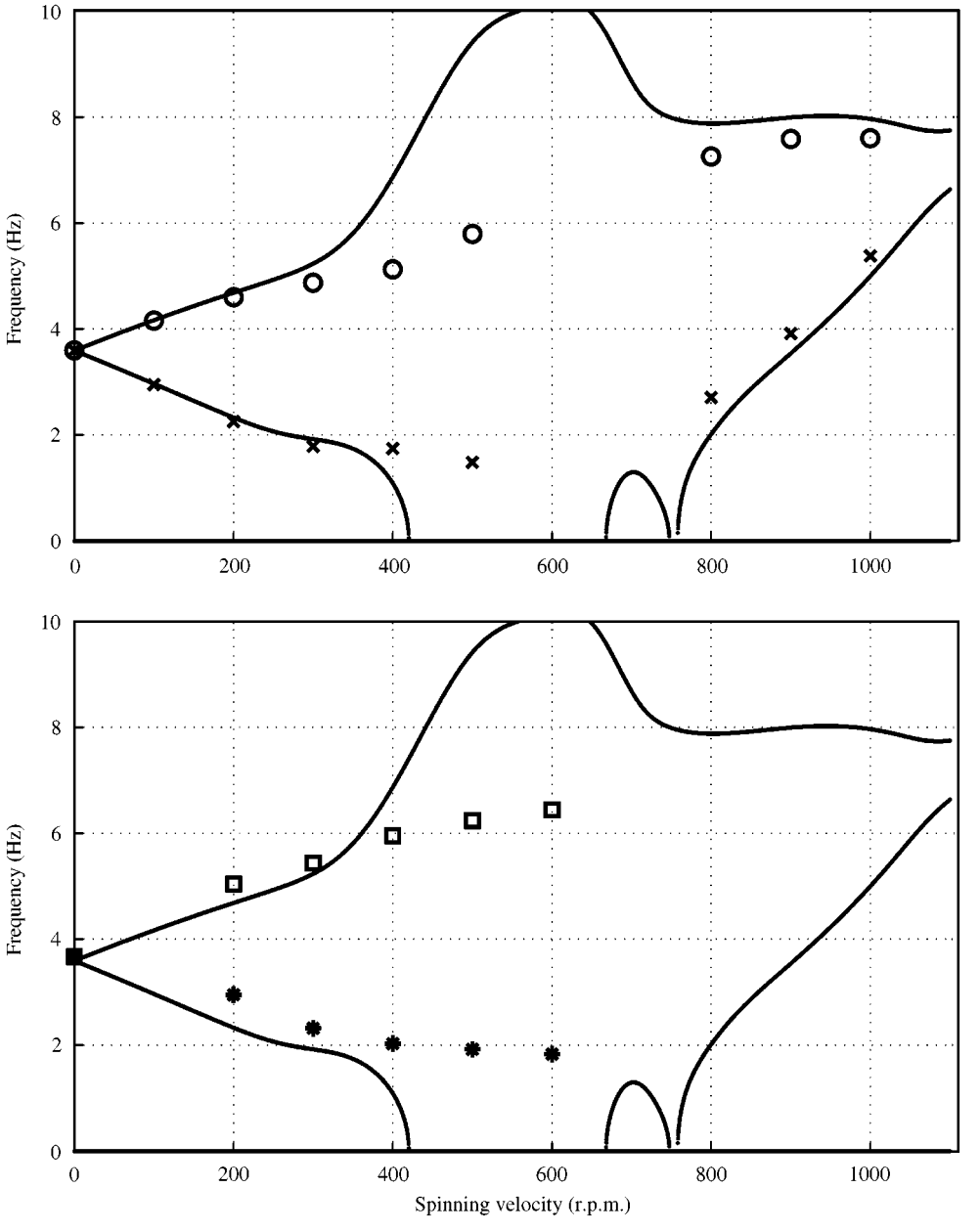

Figure 5. Comparison of modal frequencies for Configuration A: —, Linear theory; ○, first "mode" as identified from nonlinear numerical simulations; ×, second "mode" as identified from nonlinear numerical simulations; □, forward mode, experiments; ∗, Backward mode, experiments; $\varepsilon = 0{\cdot}6$.

frequency $\omega_n/(2\pi)$ and damping σ_n (real part of the corresponding eigenvalue λ_n of the flow-structure system) as a function of the rotor velocity. The modal identification was performed with the ERA method—Eigensystem Realization Algorithm (Juan 1994)—on the first set of nonlinear numerical simulations. The first 2 s of the free temporal response data, after stopping excitation, were used in the time-domain identification procedure.

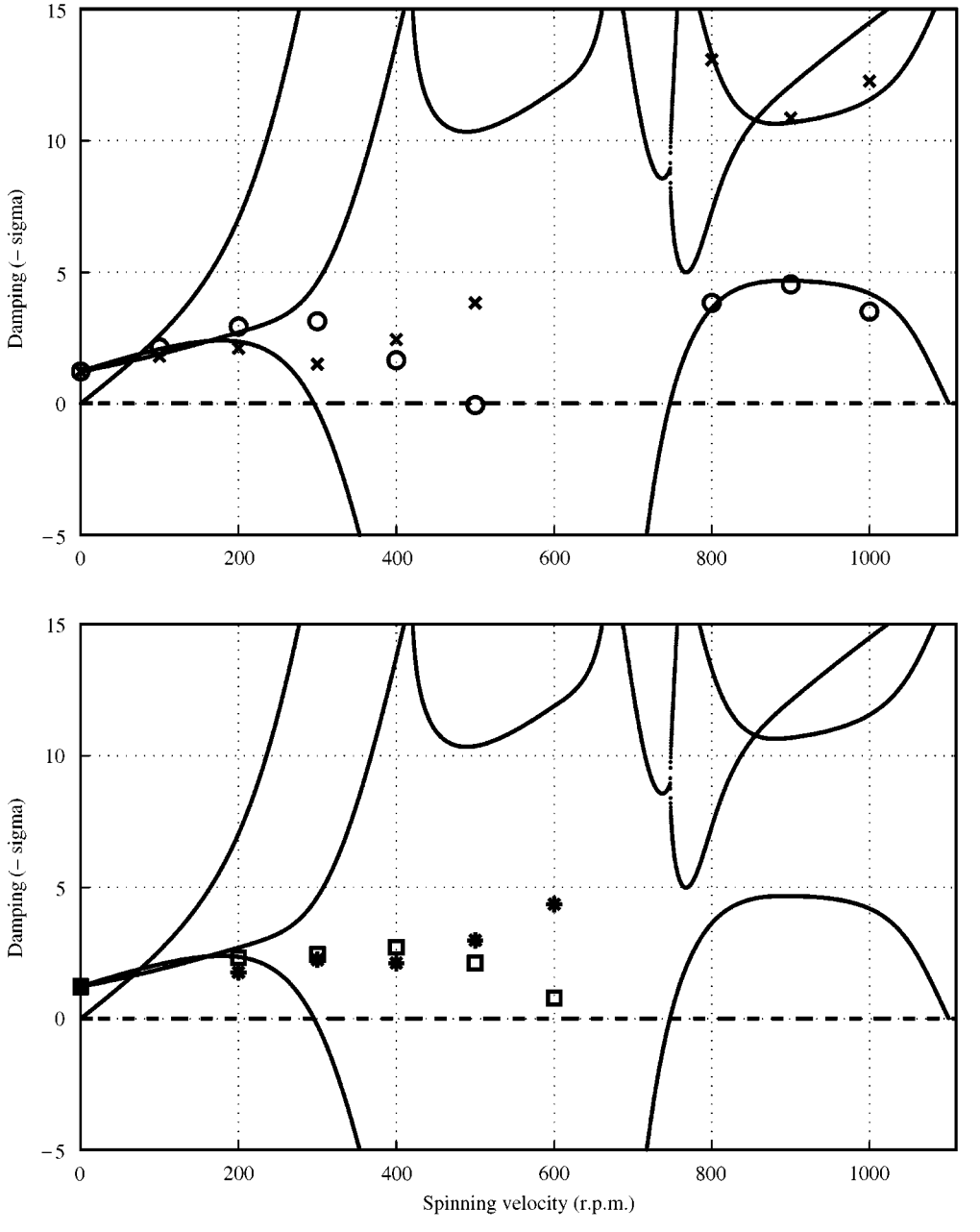

Figure 6: Comparison of modal damping for Configuration A: —, Linear theory; ○, first "mode" as identified from nonlinear numerical simulations; ×, second "mode" as identified from nonlinear numerical simulations; □, forward mode, experiments; ∗, Backward mode, experiments; $\varepsilon = 0{\cdot}6$.

Histograms of displacement responses of the second set of nonlinear simulations are presented in Figures 7 (Configuration A) and 18 (Configuration B). In these figures, we can identify the regimes with non-Gaussian responses, which stem from a nonlinear behaviour. From Figures 8 and 19, one can see the *kurtosis* and *skewness* of the dispacement responses of the second set of nonlinear numerical simulations. Estimations of these parameters were

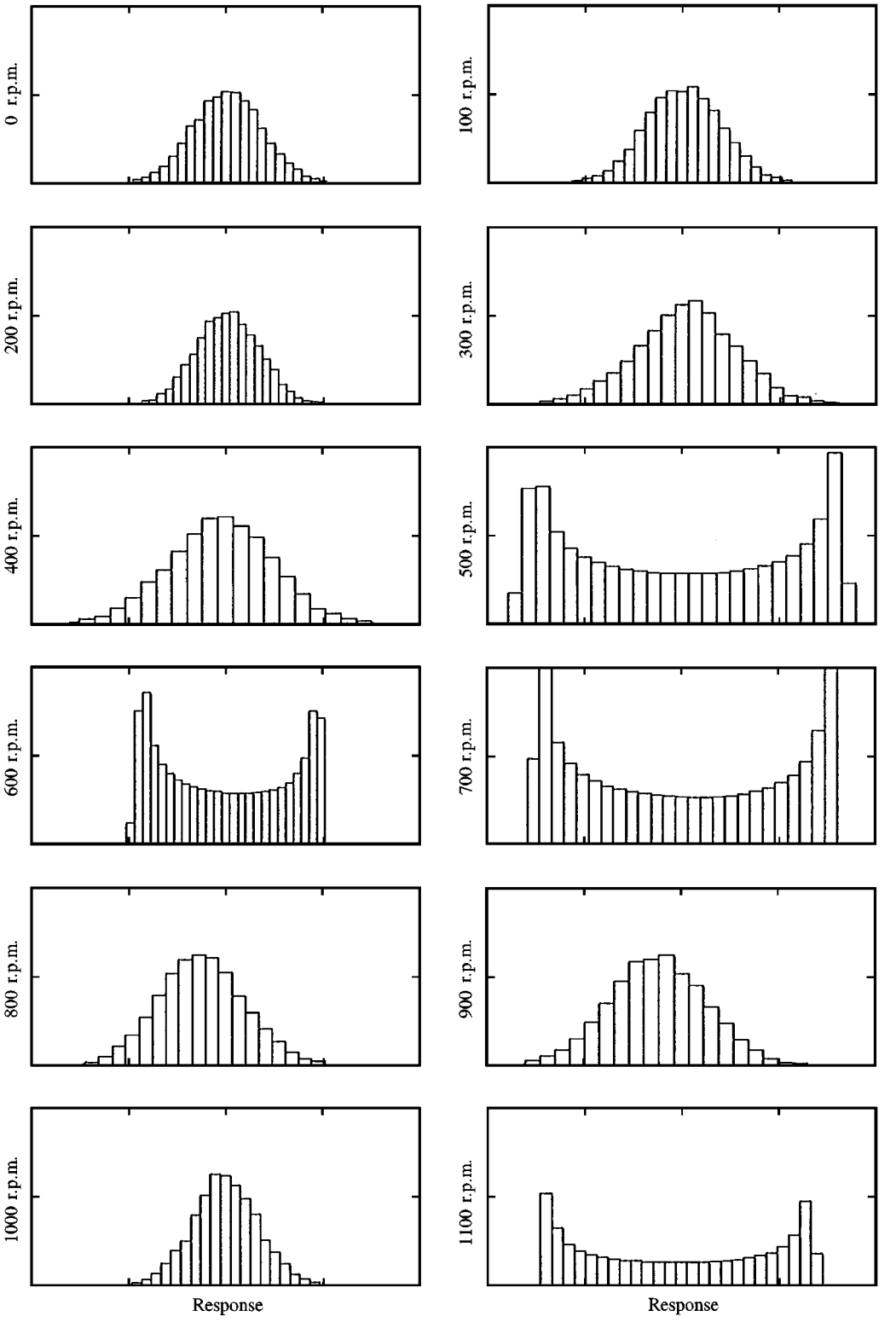

Figure 7. Histograms of the X vibratory response for Configuration A (range from 0 to 1100 r.p.m.).

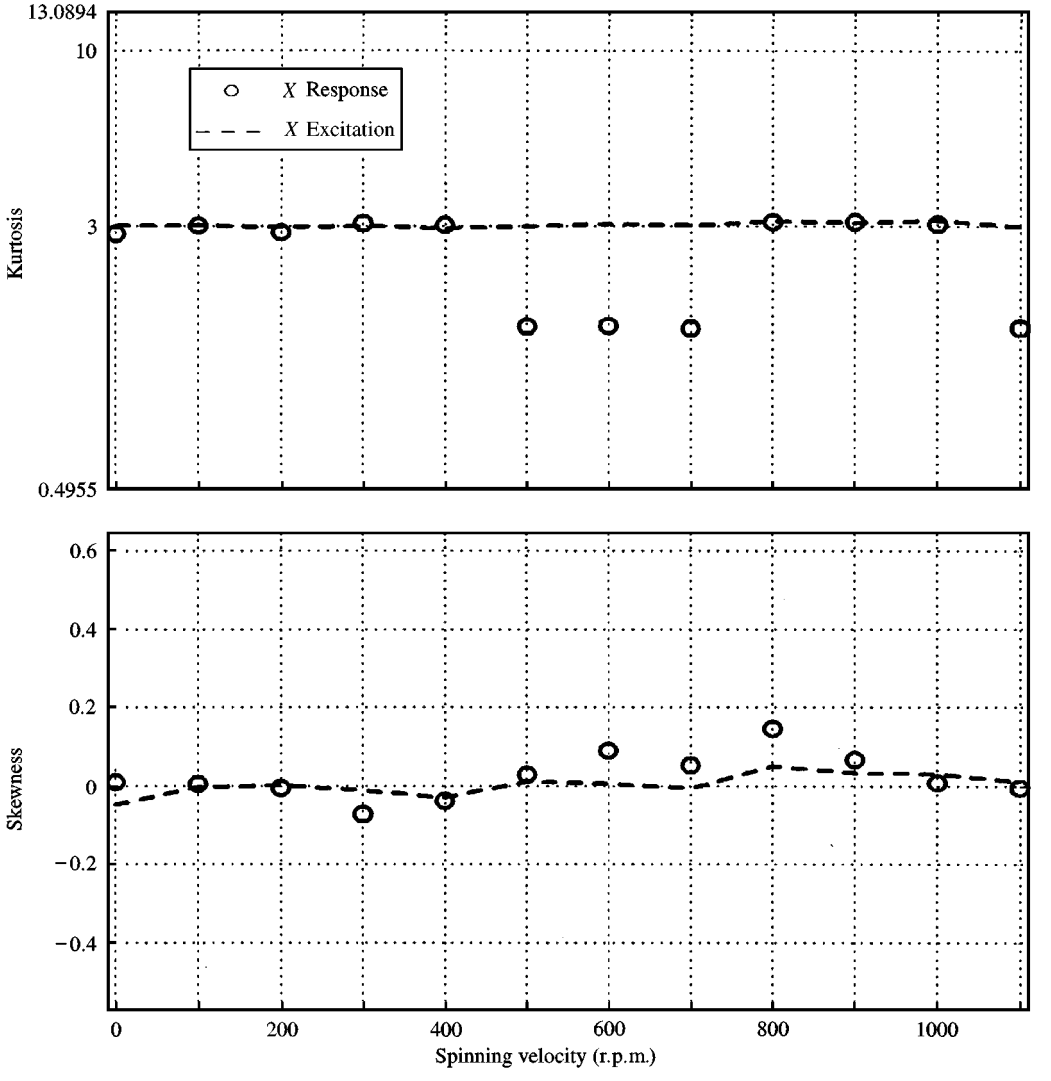

Figure 8. Kurtosis and Skewness of displacement of nonlinear simulation responses for Configuration A.

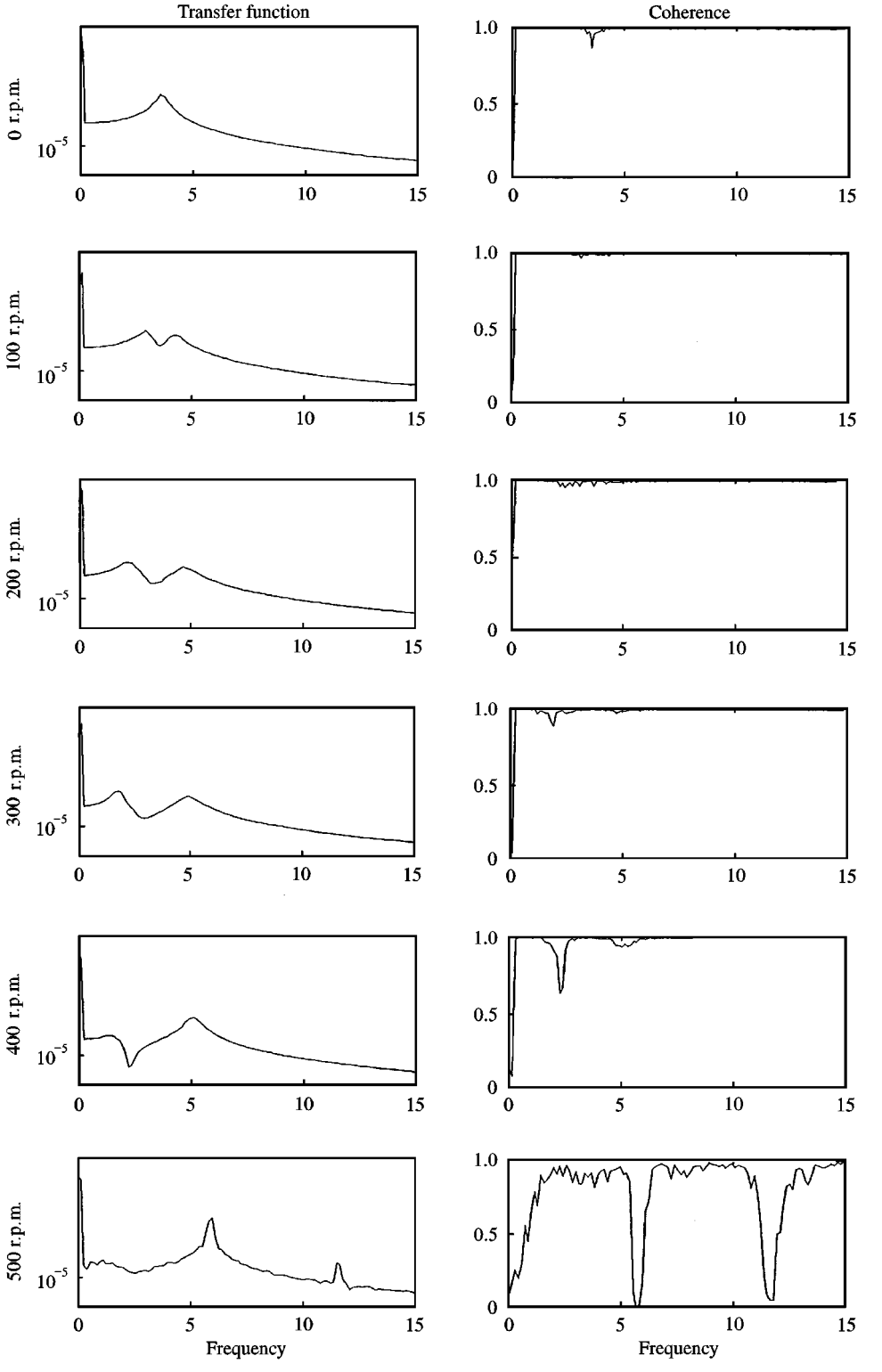

Figure 9. Transfer and coherence functions between $F_X(t)$ and $X(t)$ of nonlinear simulations for Configuration A (range from 0 to 500 r.p.m.).

computed with the following expressions (Press *et al.* 1992):

$$\text{Kurt}(x_1 \ \ldots \ x_N) = \frac{1}{N}\sum_{j=1}^{N}\left[\frac{x_j - \bar{x}}{\sigma}\right]^4,$$

$$\text{Skew}(x_1 \ \ldots \ x_N) = \frac{1}{N}\sum_{j=1}^{N}\left[\frac{x_j - \bar{x}}{\sigma}\right]^3,$$

where

$$\bar{x} = \frac{1}{N}\sum_{j=1}^{N} x_j, \quad \sigma(x_1 \ \ldots \ x_N) = \frac{1}{N}\sum_{j=1}^{N}(x_j - \bar{x})^2,$$

are respectively the mean and variance.

Values of kurtosis and skewness can be used to quantify the deviation from a Gaussian behaviour. Typically, kurtosis and skewness of a Gaussian distribution are 3 and 0, respectively.

Transfer functions and coherence functions of the nonlinear numerical simulations, computed from the second set of nonlinear numerical simulations, can be seen in Figures 9, 10 (Configuration A) and 20 (Configuration B). The coherence function between the input $F(t)$ and the output $X(t)$ is the real-valued quantity defined by

$$\gamma_{FX}(\omega) = \sqrt{\frac{|S_{FX}(\omega)|^2}{S_{FF}(\omega)S_{XX}(\omega)}},$$

where $S_{FF}(\omega)$, $S_{XX}(\omega)$ are respectively the autospectral density functions of signals $\{F(t)\}$ and $\{X(t)\}$ and $S_{FX}(\omega)$ is the cross-spectral density function between signals $\{F(t)\}$ and $\{X(t)\}$. Note that $0 \leq \gamma_{FX}(\omega) \leq 1$, and $\gamma_{FX}(\omega)$ is maximum for a constant-parameter linear system, under no-noise conditions. Therefore, low values of coherence (in the absence of noise) indicate the presence of nonlinearities on the responses (see, for instance, Bendat and Piersol 1986).

Figures 11, 12 (Configuration A) and 21 (Configuration B) show the time histories and response spectra of the main set of numerical data at several spinning velocities. The somewhat unusual two-side-frequency response representation was obtained from the Fourier transforms of the complex signals $Z(t) = X(t) + \mathrm{i}Y(t)$.

Letting $X(t) = \cos(\omega_0 t)$ and $Y(t) = \sin(\omega_0 t)$ one can observe that

$$|\mathfrak{F}(X(t) + \mathrm{i}Y(t))| = 2\pi\delta(\omega - \omega_0),$$

where δ is the Dirac delta function. So, $|\mathfrak{F}(X(t) + \mathrm{i}Y(t))|$ is a spike with the same signal of ω_0. This is the reason that this representation can be useful when one attempts to separate the whirling forward motions (positive frequencies) from the backward ones (negative frequencies). The spike at zero frequency is the result of the average eccentricity of the rotor.

In Figures 13, 14 (Configuration A) and 22 (Configuration B), one can see the orbital motions obtained during the first 2 s of free response, after stopping excitation (from the first set of numerical data).

Finally, in Figures 15 and 23 (Configuration A and B, respectively) one can see the drift as a function of the spinning velocity, predicted by the nonlinear theory (main set of data).

6.2. Discussion of Configuration A

From the identified frequencies and damping values shown in Figures 5 and 6, one can notice that the nonlinear model agrees with linear theory, in particular, from 0 to 200 r.p.m.

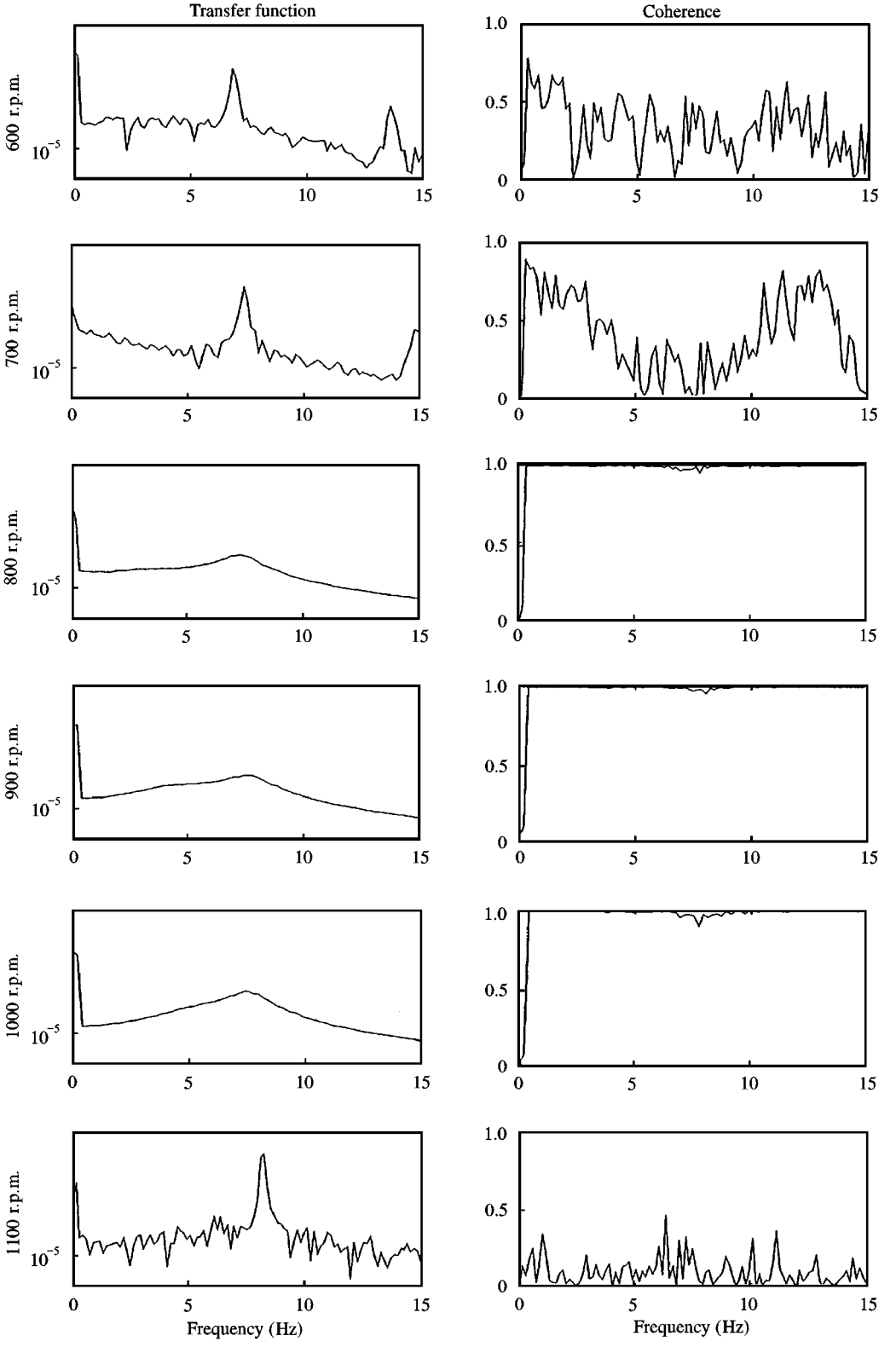

Figure 10. Transfer and coherence functions between $F_X(t)$ and $X(t)$ of nonlinear simulations for Configuration A (range from 600 to 1100 r.p.m.).

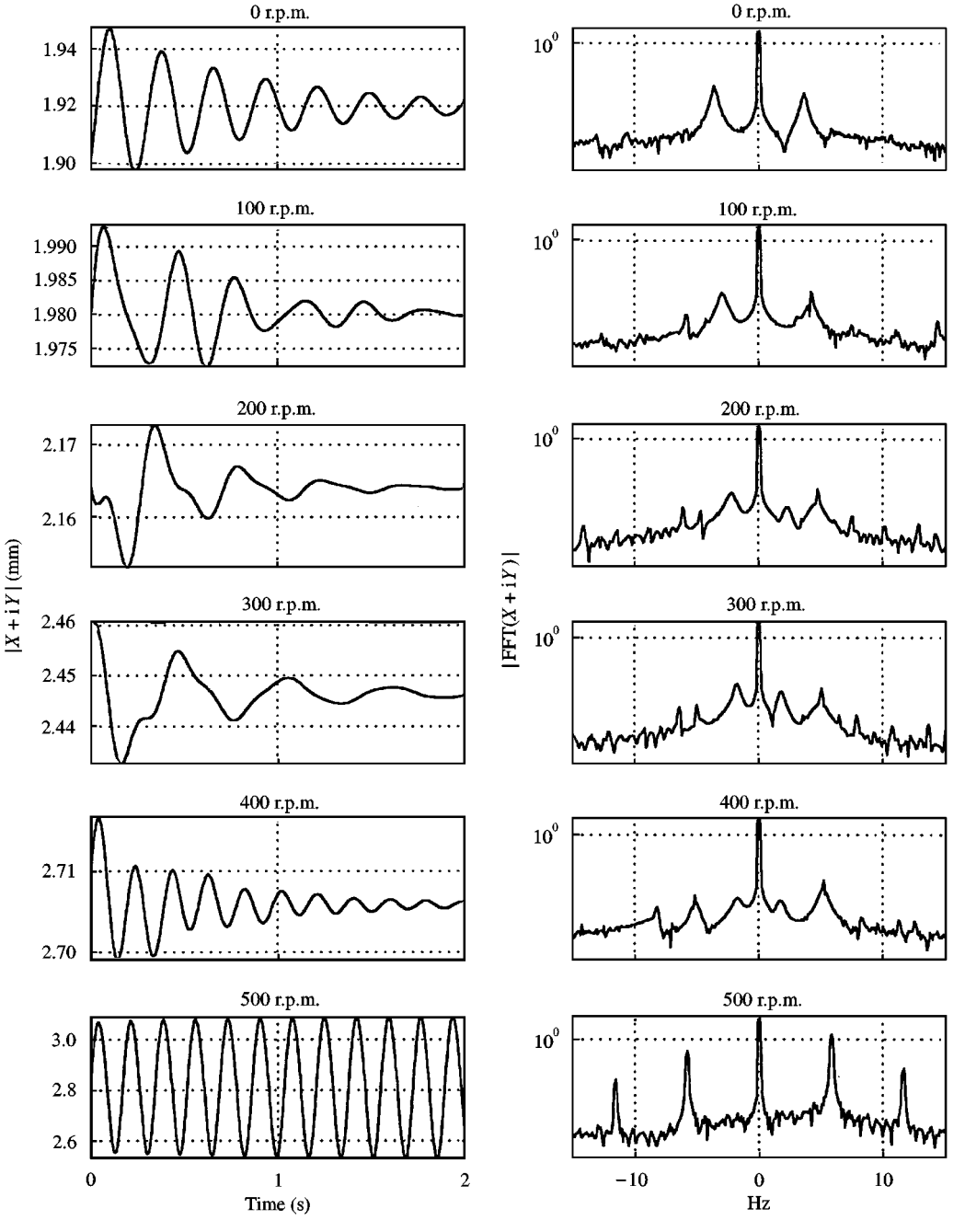

Figure 11. Computed time histories and response spectra for Configuration A (range from 0 to 500 r.p.m.).

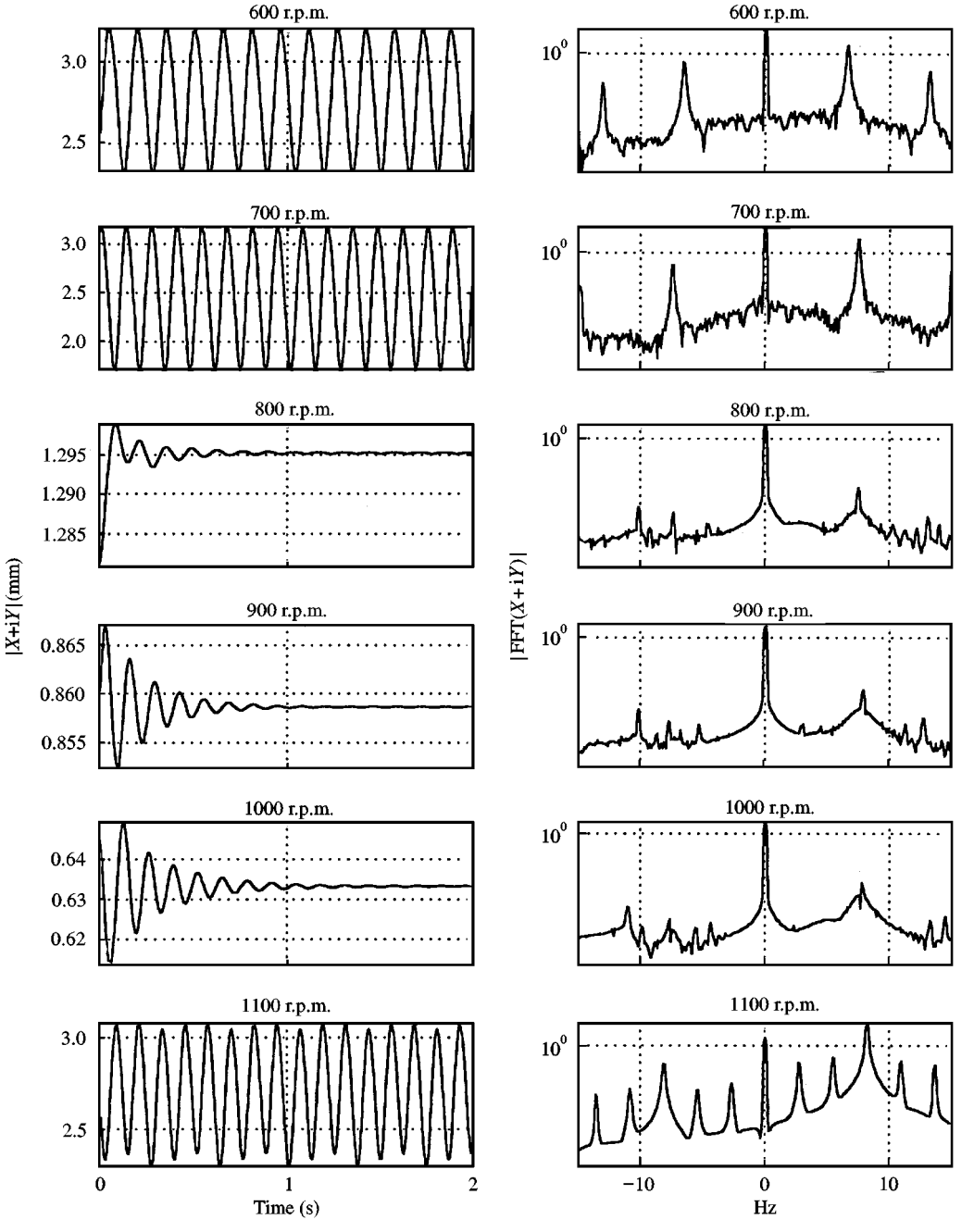

Figure 12. Computed time histories and response spectra for Configuration A (range from 600 to 1100 r.p.m.).

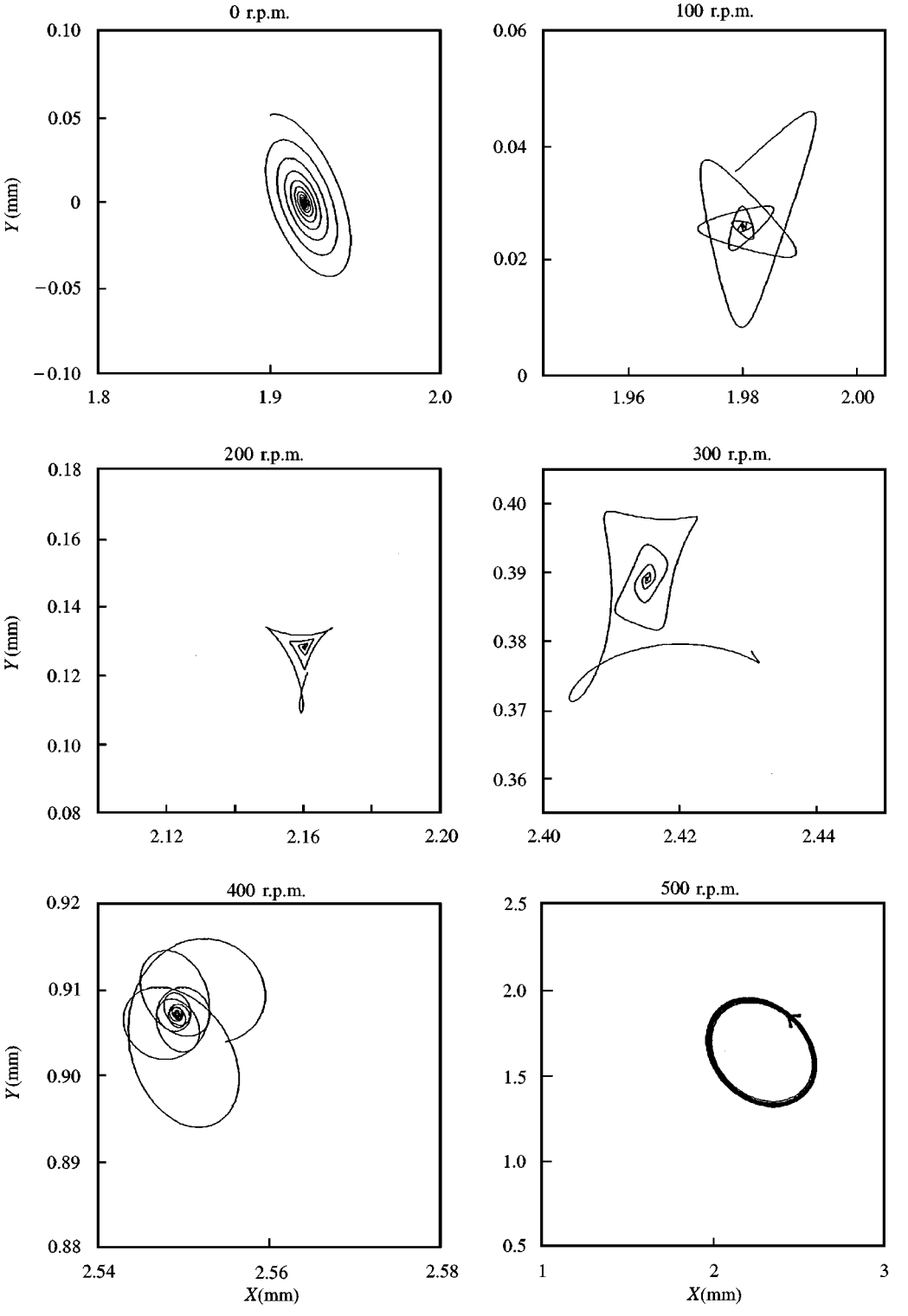

Figure 13. Computed orbital motions for Configuration A (range from 0 to 500 r.p.m.).

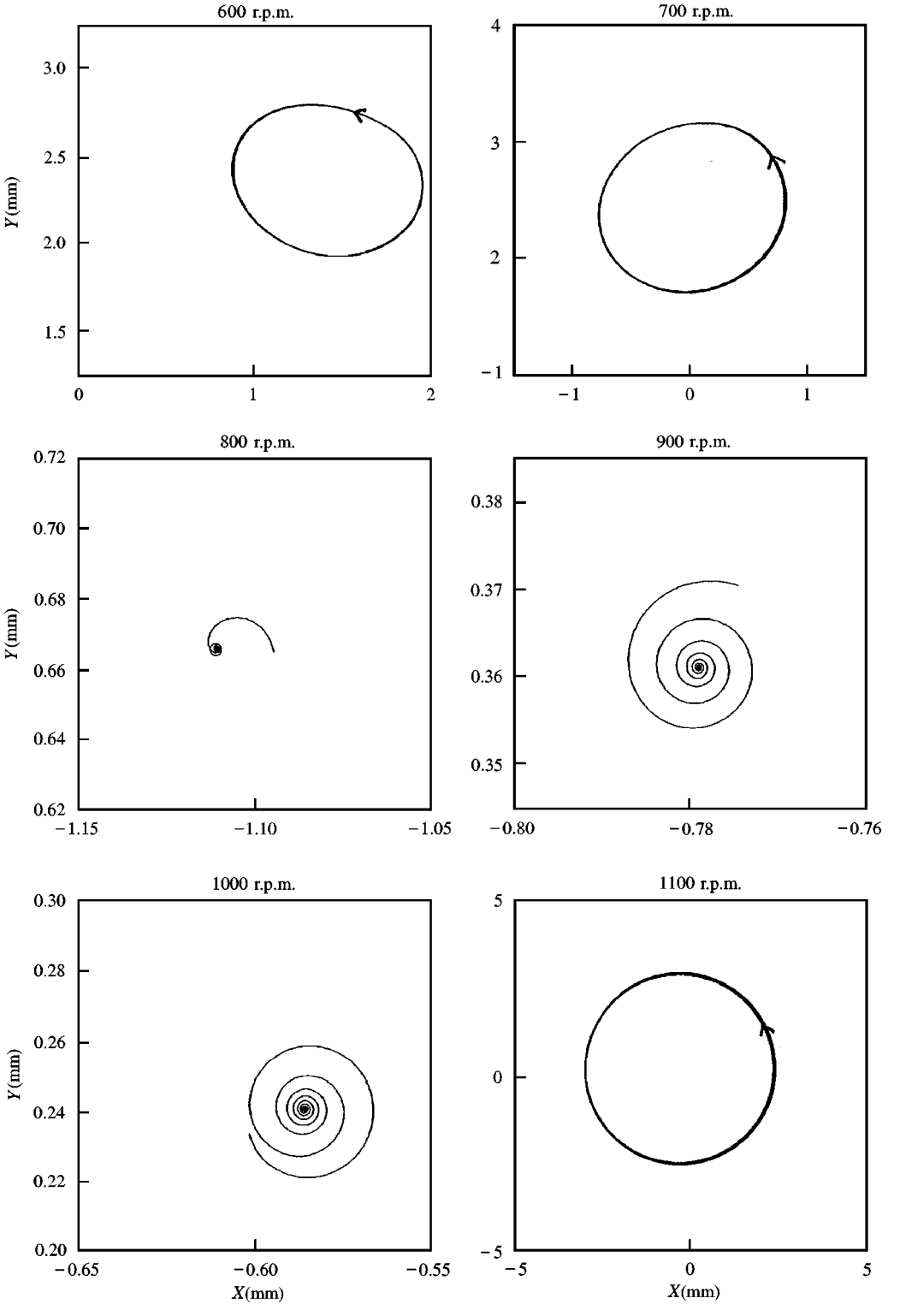

Figure 14. Computed orbital motions for Configuration A (range from 600 to 1100 r.p.m.).

Both models can give acceptable predictions of the experiments in this range, because the dynamic system displays an almost linear behaviour. This can be observed in the histograms of Figure 7, and numerically asserted from the corresponding values of the kurtosis and skewness, shown in Figure 8. We recall that a Gaussian behaviour will lead to a kurtosis of 3 and skewness of 0.

Above this range and below 800 r.p.m. the system becomes linearly unstable. Nonlinear forces prevail, and so only numerical nonlinear simulations yield results which are similar to experiments. This can be confirmed (namely in the identified frequencies) in the range between 300 and 400 r.p.m. One can observe in Figure 9 a progressive deterioration in the values of coherence of response, in this range. The severe nonlinear behaviour from 500 to 700 r.p.m. is highlighted by the shape of the histogram plots, in Figure 7, as well as by the corresponding values of kurtosis in Figure 8.

One can observe a similar evolution of damping between the non-linear numerical simulations and the experiments in Figure 6. Notice that, although the identified damping is positive in the range below 500 r.p.m., these are only apparent values, because nonlinear effects prevail after the linear instability arising at 300 r.p.m. Indeed, linear theory and nonlinear numerical simulations predict instability respectively at 300 and 500 r.p.m. Experimental instability was observed at about 650 r.p.m.

Note that, after the linear restabilization at 750 r.p.m., the linear and nonlinear models agree again very well (see Figures 5 and 6). The linear behaviour of the system in this range is confirmed by the corresponding histograms of Figure 7, by the values of kurtosis and skewness in Figure 8 or by the high values of coherence displayed in Figure 10.

The limit cycles obtained in the 500, 600 and 700 r.p.m. range are shown in Figures 11–14, as well as the stable free responses at lower velocities. Observe that the limit cycles correspond to forward orbits. Note that, in experiments, this configuration became unstable in the *forward whirling mode* after 650 r.p.m. (Grunenwald *et al.* 1996). Restabilization at 750 r.p.m. can also be observed in Figures 12 and 14. No experimental dynamic results were available in this range.

The rotor drift, as a function of the spinning velocity, is shown in Figure 15. For rotors under moderate fluid confinement, the drift is mostly due to a Bernoulli effect, but is also affected by the dissipative forces. The drift predicted by the nonlinear theory agree reasonably well with experiments in the range up to 700 r.p.m. (no experimental data is available beyond 800 r.p.m.). The same type of qualitative behaviour was experimentally observed by Grunenwald *et al.* (1996) at different eccentric configurations. One should note that the finite length of the rotor may significantly affect the results, which might account for the discrepancies on the drift angle. At present, these effects are very difficult to quantify.

6.3. Discussion of Configuration B

In Figures 16 and 17, we note again that nonlinear simulations and linear theory agree reasonably well in the range below 400 r.p.m. Both models give acceptable predictions of the experimental behaviour, in this range. This accounts for the linear dynamic of system, which is attested by the histograms in Figure 18, and the values of kurtosis, skewness and coherence can be observed in Figures 19 and 20, respectively.

Above this range, the nonlinear numerical simulations still yield results which are similar to experiments, with respect to the identified frequencies, as we can observe in Figure 16. The identified damping values from the nonlinear simulations are somewhat lower than in the experiments, as shown in Figure 17. We can also, verify that, from 200 to 400 r.p.m., the apparent damping values of the *forward whirling mode* and of the *backward whirling mode* are reversed in simulations and experiments. This may be due to three-dimensional flow

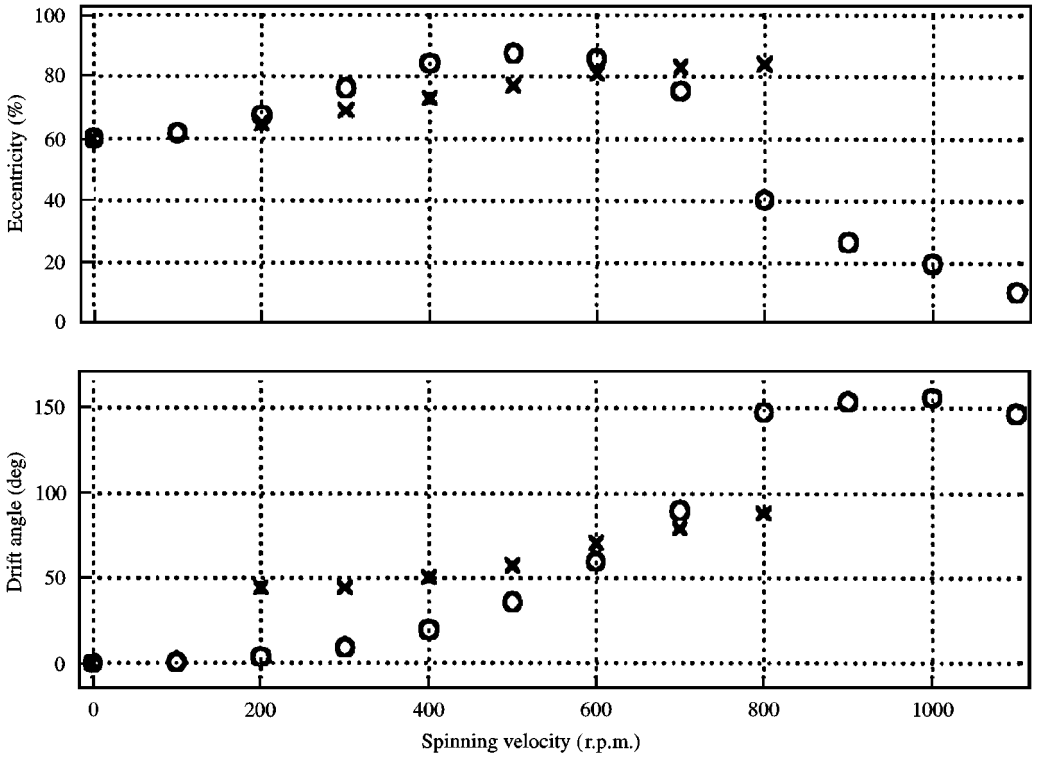

Figure 15. Magnitude and angle of the steady rotor drift for Configuration A: ○, nonlinear simulations; ×, experiments.

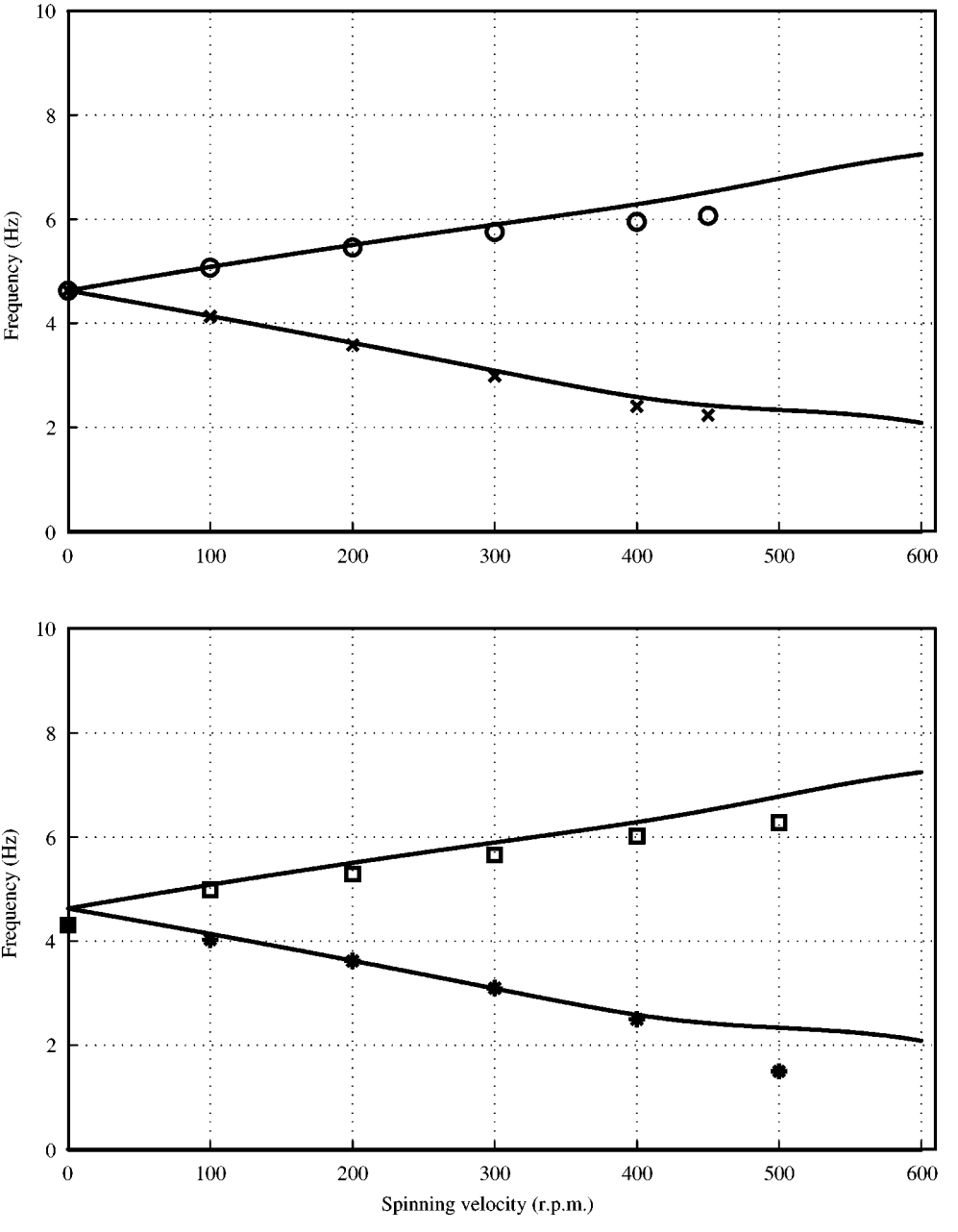

Figure 16. Comparison of modal frequencies for Configuration B: —, Linear theory; ○, first "mode" as identified from nonlinear numerical simulations; ×, second "mode" as identified from nonlinear numerical simulations; □, forward mode, experiments; ∗, Backward mode, experiments; $\varepsilon = 0{\cdot}6$.

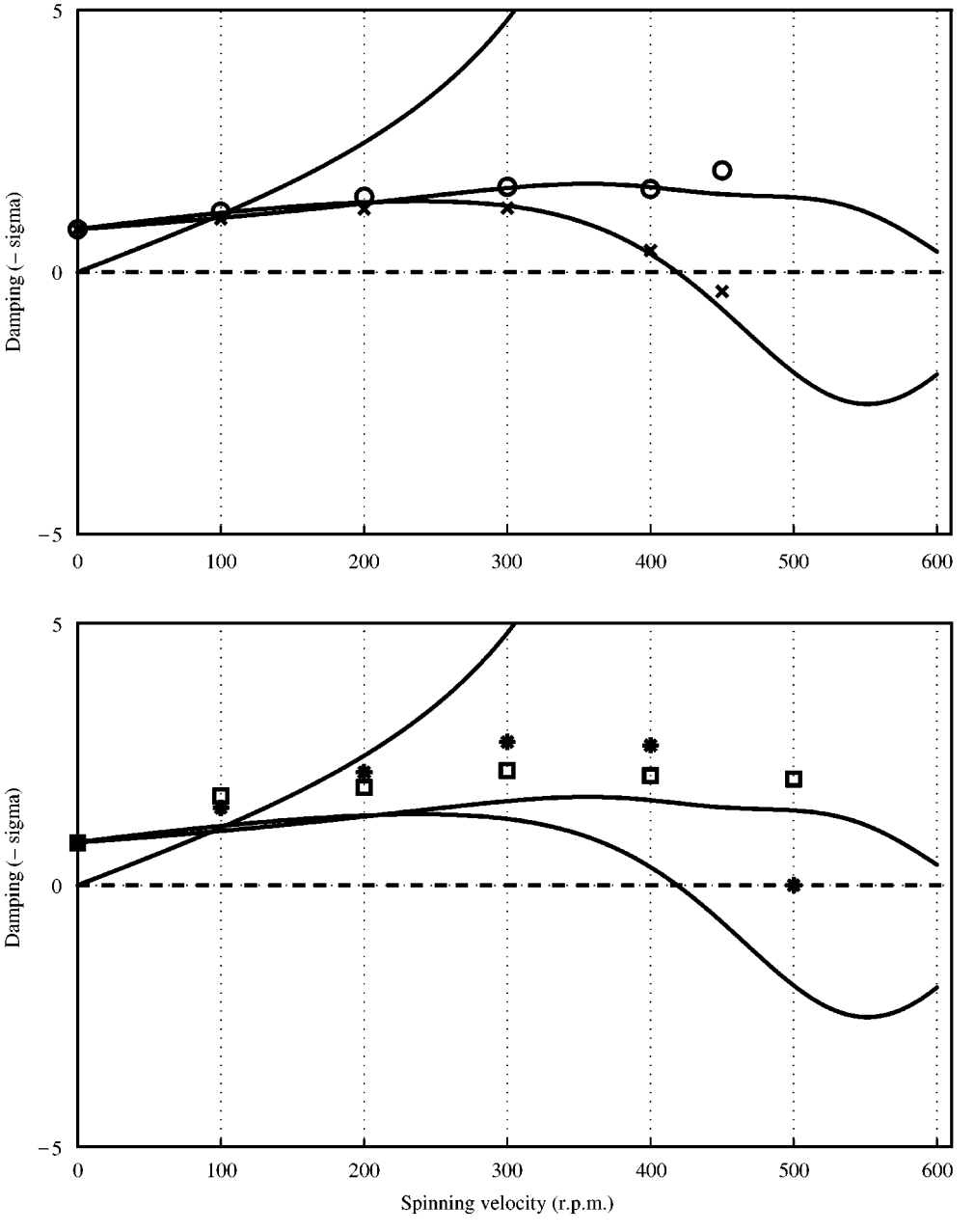

Figure 17. Comparison of modal damping for Configuration B: —, Linear theory; ○, first "mode" as identified from nonlinear numerical simulations; ×, second "mode" as identified from nonlinear numerical simulations; □, forward mode, experiments; ∗, Backward mode, experiments; $\varepsilon = 0{\cdot}6$.

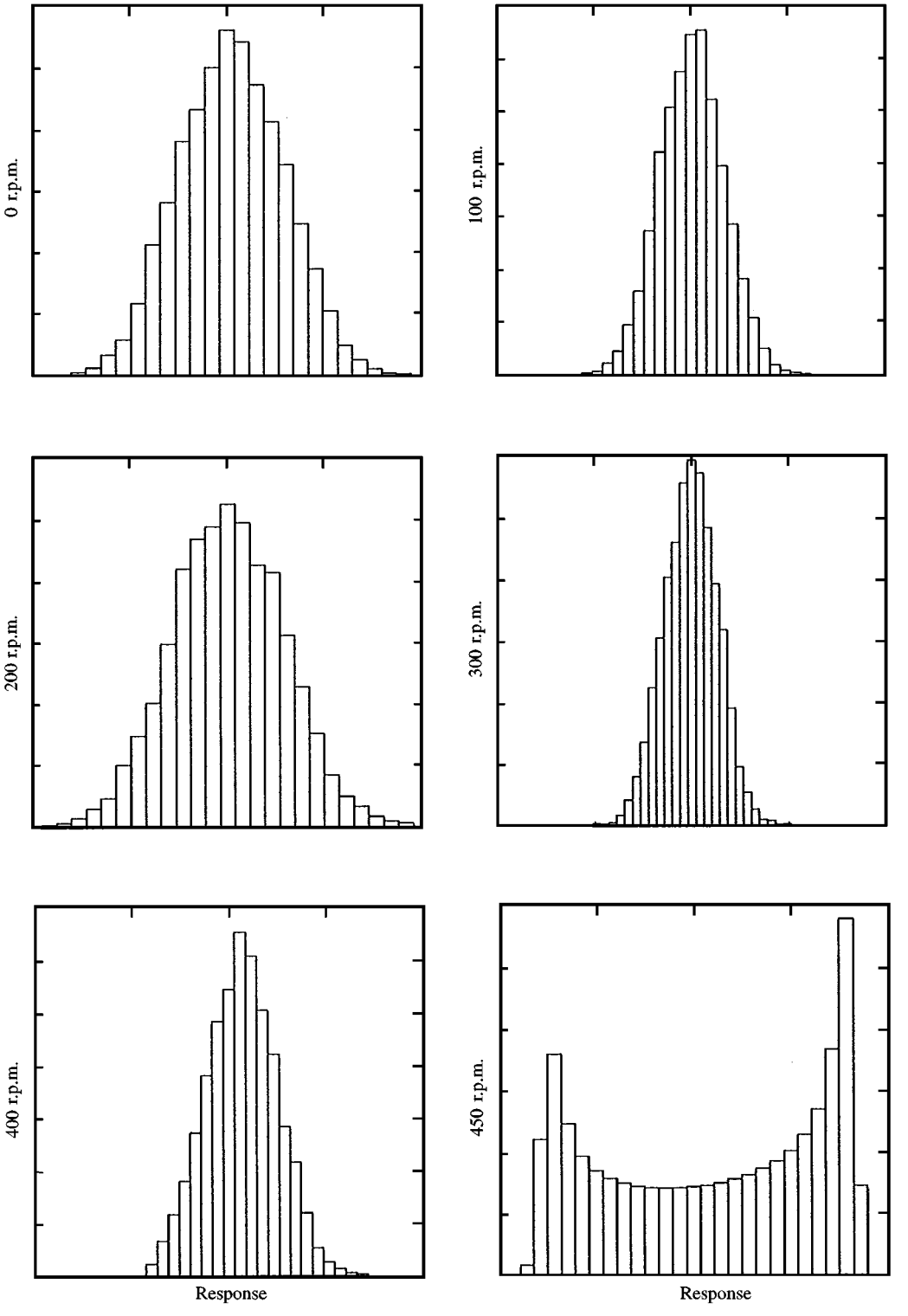

Figure 18. Histograms of the X vibratory response for Configuration B (range from 0 to 450 r.p.m.).

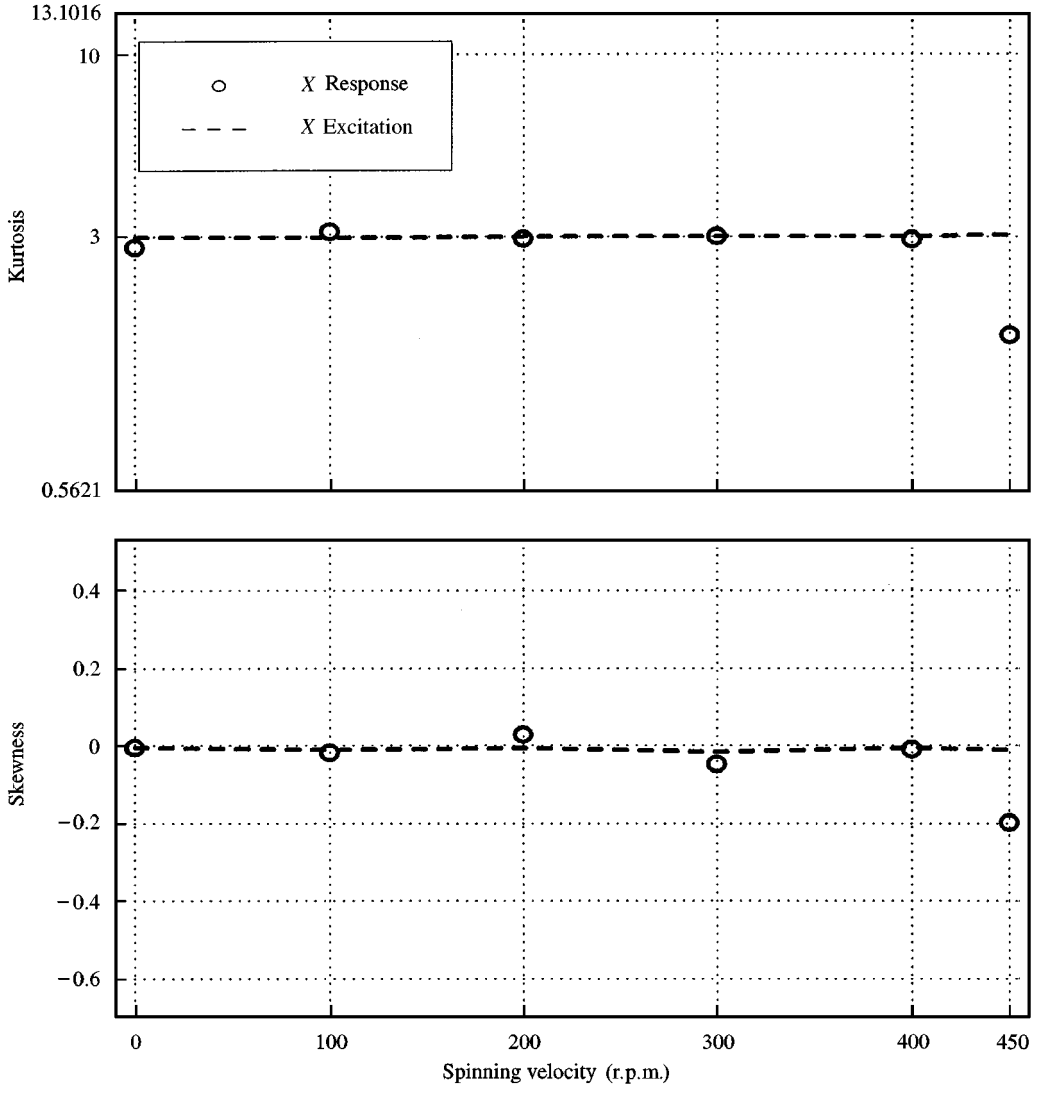

Figure 19. Kurtosis and skewness of displacement of nonlinear simulation responses for Configuration B.

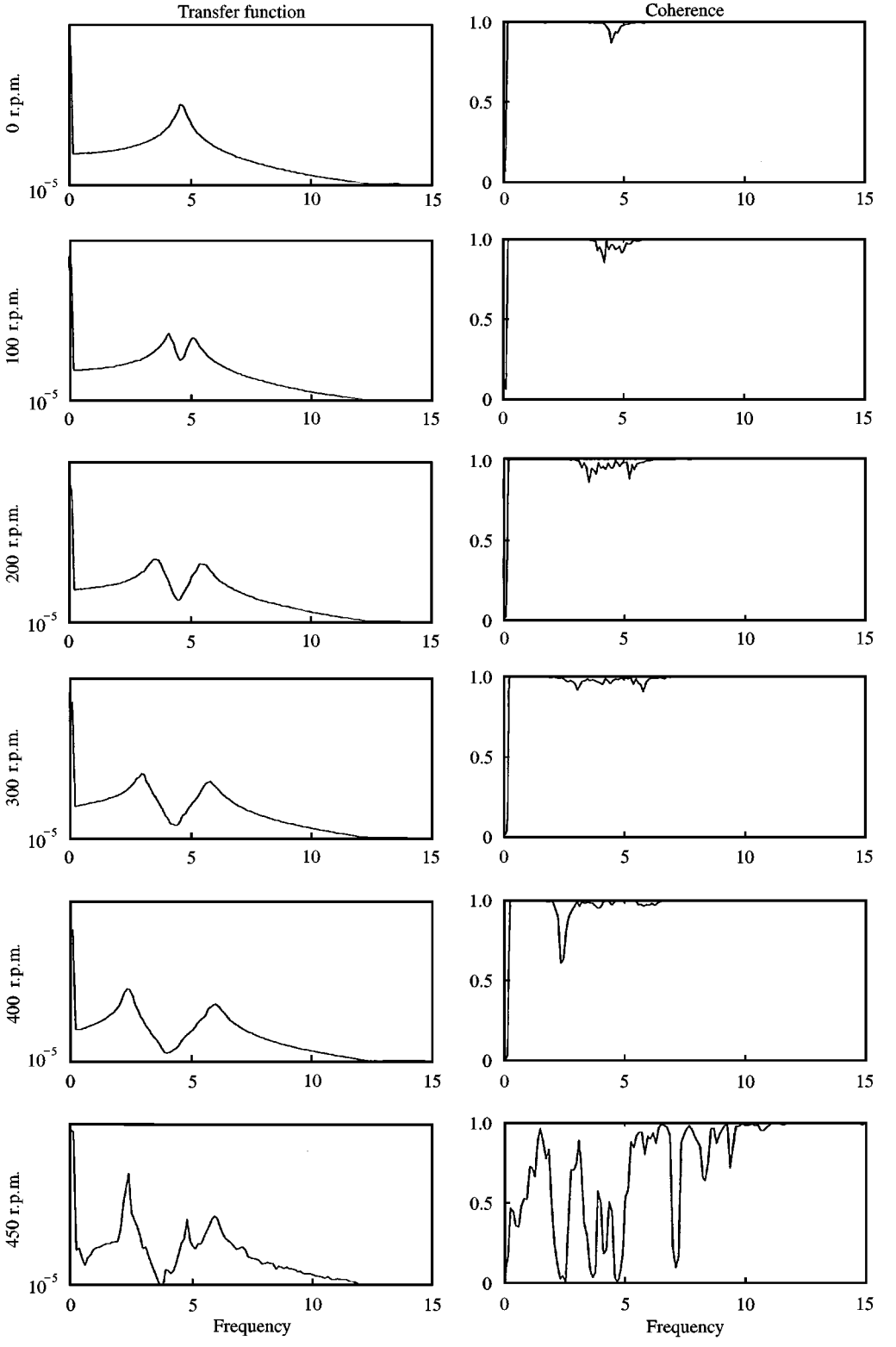

Figure 20. Transfer and coherence functions between $F_X(t)$ and $X(t)$ of nonlinear simulations for Configuration B (range from 0 to 450 r.p.m.).

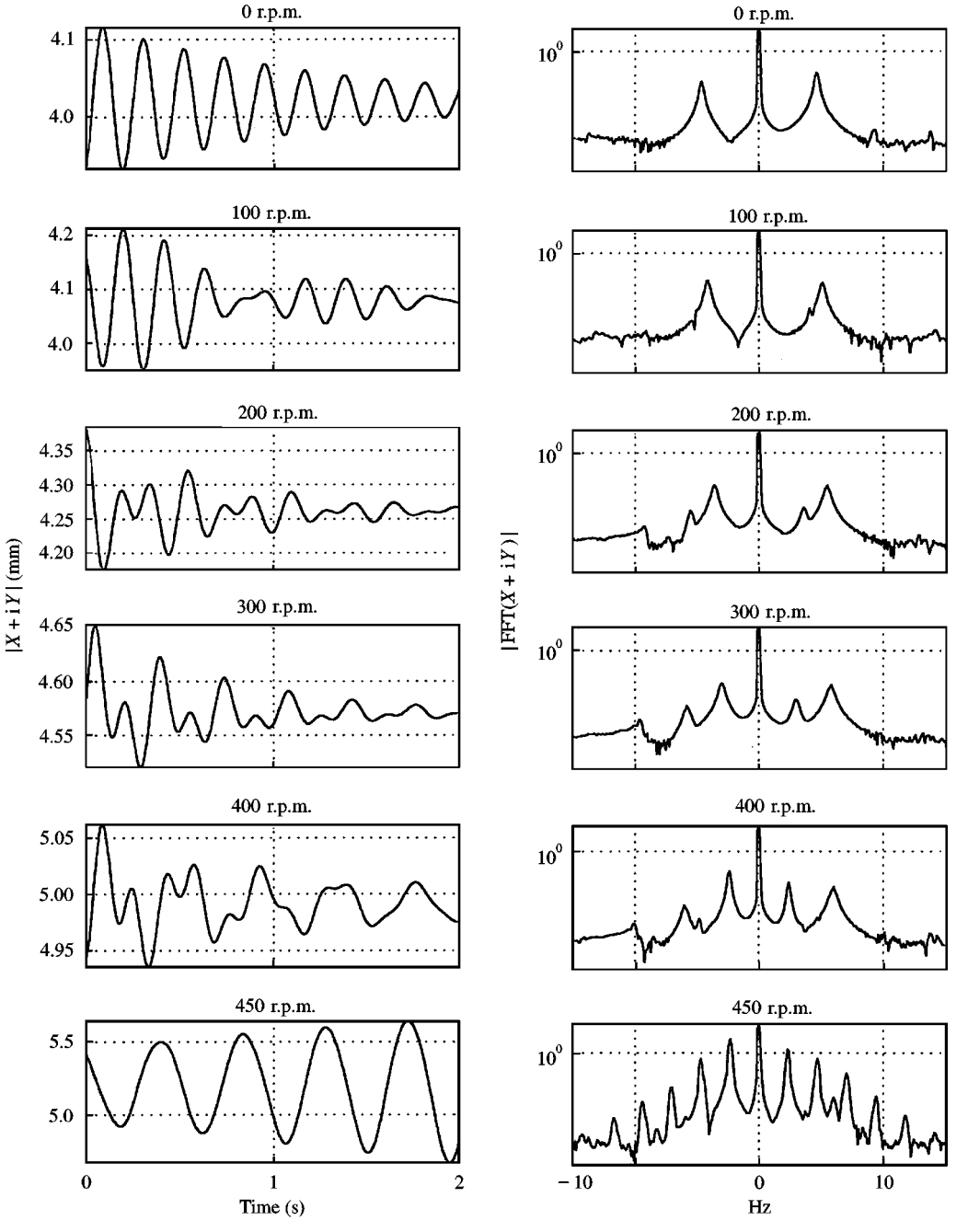

Figure 21. Computed time histories and response spectra for Configuration B (range from 0 to 450 r.p.m.).

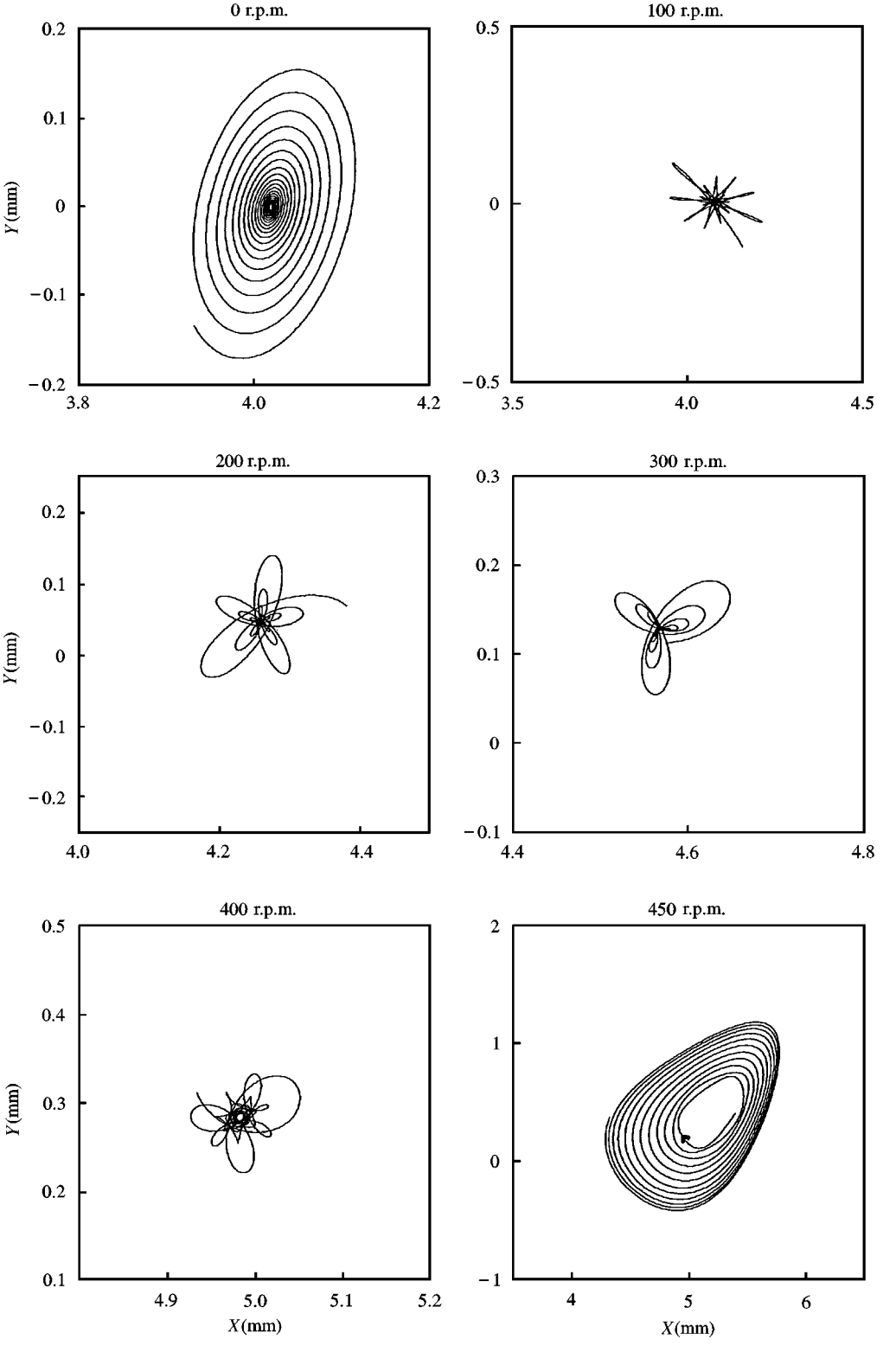

Figure 22. Computed orbital motions for Configuration B (range from 0 to 450 r.p.m.).

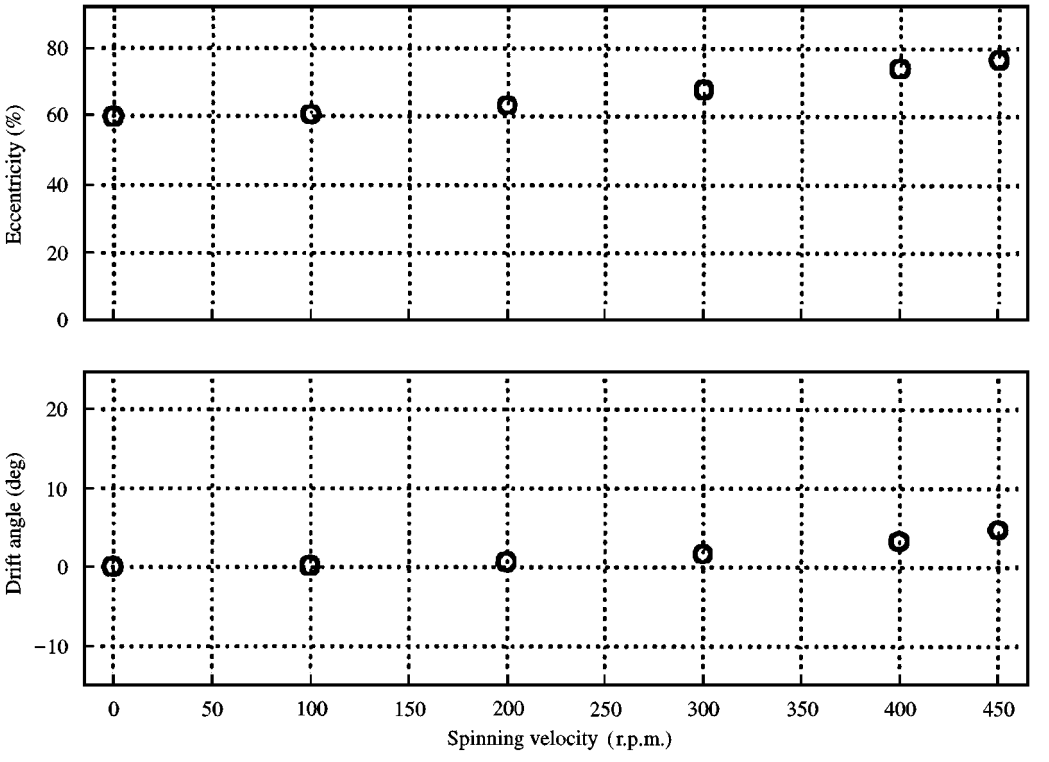

Figure 23. Magnitude and angle of the steady rotor drift for Configuration B: (○, nonlinear simulations).

effects not accounted by the theoretical assumptions of our model. Indeed, Configuration B presents a higher reduced gap ($\delta \simeq 0{\cdot}15$) than Configuration A, leading to a higher value of the ratio H/L. Therefore, 3-D flow effects are certainly more significant in the experiments with Configuration B.

Linear theory and numerical simulations predict instability respectively at 425 and 450 r.p.m., as we can seen in Figure 17. In experiments this configuration became also unstable in the *backward whirling mode*, but at about 500 r.p.m. The nonlinear behaviour after instability is attested to by the histograms in Figure 18 and by the plots in Figure 21. Also, we can observe in Figure 22 the backward limit cycle in this range, as predicted by the nonlinear simulations at 450 r.p.m.

The rotor drift, for this configuration (Figure 23) and for Configuration A (Figure 15) displays a similar behaviour, between 0 and 500 r.p.m. (before the occurrence of instability).

7. CONCLUSIONS

In a previous paper (Antunes *et al.* 1999) a theoretical model was developed for nonlinear *planar* motions—motions $X(t)$ taking place in one single direction—of rotors under fluid confinement using simplified flow equations on the gap-averaged fluctuating quantities.

Following a similar aproach, the nonlinear theoretical model was here extended to cope with *orbital* rotor motions—motions $X(t)$ and $Y(t)$ taking place in two different ortogonal directions, by developing an exact formulation for the two-dimensional dynamic flow forces.

Besides the fact our nonlinear orbital model can predict the rotor drift (and so the dynamic eccentricity) which strongly governs the system dynamics and whose knowledge is essential in linear predictions, the results obtained show the following:

(a) The nonlinear model and linear theory agree when the spinning velocity or the dynamic eccentricity are low enough, e.g. the linear simplifying assumptions are fulfilled. However, the range in which the system behaves linearly is small (0–200 r.p.m. in both configurations).

(b) In a range of moderate spinning velocities and/or significant dynamic eccentricity (200–500 r.p.m. in Configuration A and 200–400 r.p.m. in Configuration B), our results suggest that experiments were performed under linear instability, the response being stabilized by nonlinear effects. This fact explains the significant differences observed between experiments and linear theory. In these regimes, the system behaves nonlinearly, and so only the nonlinear model agrees with experiments, in particular concerning the identified response frequencies. However, nonlinear numerical simulations lead to a lower apparent damping values than the experimentally identified. This may be due to three-dimensional flow effects not accounted for by the theoretical assumptions of our model.

(c) Our nonlinear model is conservative (as a result from the lower damping exhibited). Instability is predicted at 10–20% lower velocities than the occurrence of experimental instabilities. Observe that the correct post-stable whirling instabilities (forward or backward limit cycles), were also well predicted by the nonlinear flow model.

In spite of some anomalous results in the identified damping in Configuration B, most probably due to 3-D flow effects mentioned before, one can conclude that our nonlinear flow model leads to much better predictions of the rotor dynamics.

Experimental work is currently being done to further assess the validity of the present nonlinear theory.

ACKNOWLEDGMENTS

Thanks to Aurelian Tissot, from the Université Technologique de Troyes (UTT/France), for the interesting discussions and valuable debugging work.

References

Antunes, J., Axisa, F. & Grunenwald, T. 1996 Dynamics of rotors immersed in eccentric annular flow. Part 1—theory. *Journal of Fluids and Structures* **10,** 893–918.

Antunes, J., Mendes, J., Moreira, M. & Grunenwald, T. 1999 A theoretical model for nonlinear planar motions of rotors under fluid confinement. *Journal of Fluids and Structures* **13,** 103–106.

Axisa, F. & Antunes, J. 1992 Flexural vibrations of rotors immersed in dense fluids. Part 1—theory. *Journal of Fluids and Structures* **6,** 3–21.

Bendat, J. S. & Piersol, A. J. 1986 *Random Data.* New York: John Wiley & Sons.

Black, H. 1969 Effects of hydraulic forces in annular pressure seals on the vibrations of centrifugal pump rotors. *I. Mech. E. Journal of Mechanical Engineering Science* **11,** 206–213.

Childs, D. 1983 Finite length solutions for rotordynamic coefficients of turbulent annular seals. *ASME Journal of Lubrication Technology* **105,** 437–444.

Fritz, R. 1970 The effects of an annular fluid on the vibrations of a long rotor. Part 1—theory. *ASME Journal of Basic Engineering* **92,** 923–929.

Goodwin, M. J. 1989 *Dynamics of Rotor-Bearing Systems.* London: Unwin Hyman.

Grunenwald, T. 1994 Comportement vibratoire d'arbres de machines tournantes dans un espace annulaire de fluide de confinement modéré. Doctoral Thesis, University of Paris.

Grunenwald, T., Axisa, F. & Antunes, J. 1991 Rotor vibration under fluid confinement: analysis of dissipative phenomena and stability. *Journal of Fluids and Structures* **10,** 919–944.

GRUNENWALD, T., AXISA, F., BENNETT, G. & ANTUNES, J. 1996 Dynamics of rotors immersed in eccentric annular flow. Part 2 - Experiments. *Journal of Fluids and Structures* **10,** 919–944.

HIRS, G. G. 1973 A bulk-flow theory for turbulence in lubricant films. *ASME Journal of Lubrication Technology* **95,** 137–146.

JUAN, J. 1994 An Eigensystem realization algorithm for modal parameter identification and modal reduction. *AIAA Journal of Guidance, Control and Dynamics* **8,** 620–697.

MOREIRA, M., ANTUNES, J. & PINA, H. 2000 An improved linear model for rotors subject to dissipative annular flows. (*7th International Conference on Flow Induced Vibrations*, Lucern, Switzerland) (submitted).

NELSON, C. 1985 Rotordynamic coefficients for compressible flows in tapered annular seals. *ASME Journal of Tribology* **107,** 318–325.

NORDMANN, R., DIETZEN, F. & WEISER, H. 1989 Calculation of rotordynamic coefficients and leakage for annular gas seals by means of finite difference techniques. *ASME Journal of Tribology* **111,** 545–552.

PRESS, W., FLANNERY, B., TEUKOLSKY, S. & VETTERLING, W. 1992 *Numerical Recipes*: *The Art of Scientific Computing*. Cambridge: University Press.

RAMSDEN, J., RITCHIE, G. & GUPTA, J. 1974 The Vibrational response characteristics of a design for the sodium pumps of the commercial Fast Reactor. *Proceedings I. Mech. E. Fluid Machinery and Nuclear Energy Groups Convention*: *Pumps For Nuclear Power Plant*. Bath, April 1974. Paper C107/74, pp. 187–196.

RAMSDEN, J., JONES, H. & COWKING, E. 1975 Vibration of the P.F.R. primary sodium pumps**.** *Vibrations and Noise in Pump, Fan and Compressor Installations*. Southampton, September 1975. Paper C103/75, pp. 21–33.

SHAMPINE, L. F. 1994 *Numerical Solution of Ordinary Differential Equations*. New York: Chapman & Hall.

WENDT, F. 1933 Turbulente Stomungen zwischen zwei Rotierenden konaxialen Zylindern. *Ingenieur Archiv* **4,** 577–595.

APPENDIX A: INTEGRAL FACTORS

A list is given below, without comment.

$$\mathbb{I}_1^X(t) \equiv \int_0^{2\pi} \frac{\partial(hu)}{h\partial t} \sin\theta \, \mathrm{d}\theta$$

$$= R(\ddot{X}G_1^{20} - \ddot{Y}G_1^{11} + \dot{C}G_1^{10}), \tag{A1}$$

$$\mathbb{I}_2^X(t) \equiv \int_0^{2\pi} \frac{\partial(hu^2)}{h\partial\theta} \sin\theta \, \mathrm{d}\theta$$

$$= 2R^2(((\dot{X})^2 - (\dot{Y})^2)G_2^{21} + 2\dot{X}\dot{Y}G_2^{30})$$
$$+ 2R^2(-\dot{X}\dot{Y}G_2^{10} + C(\dot{X}G_2^{11} + \dot{Y}G_2^{20}))$$
$$- R^2((\dot{X})^2 XG_3^{40} + X(\dot{Y})^2 G_3^{22} - 2X\dot{X}\dot{Y}G_3^{31})$$
$$- R^2(C^2 XG_3^{20} + 2CX(\dot{X}G_3^{30} - \dot{Y}G_3^{21}))$$
$$- R^2(-(\dot{X})^2 YG_3^{31} - Y(\dot{Y})^2 G_3^{13} + 2\dot{X}Y\dot{Y}G_3^{22})$$
$$- R^2(-C^2 YG_3^{11} - 2CY(\dot{X}G_3^{21} - \dot{Y}G_3^{12})), \tag{A2}$$

$$\mathbb{I}_3^X(t) \equiv \int_0^{2\pi} \frac{(\tau_s + \tau_r)}{h} \sin\theta \, \mathrm{d}\theta$$

$$= \rho f \Omega R^2(\dot{X}G_2^{20} - \dot{Y}G_2^{11} + CG_2^{10}) - \frac{1}{2}\rho f \Omega^2 R^2 G_1^{10}; \tag{A3}$$

$$\mathbb{I}_1^Y(t) \equiv \int_0^{2\pi} \frac{\partial(hu)}{h\partial t} \cos\theta \, \mathrm{d}\theta = \mathrm{R}(\ddot{X}G_1^{11} - \ddot{Y}G_1^{02} + \dot{C}G_1^{01}), \tag{A4}$$

$$\mathbb{I}_2^Y(t) \equiv \int_0^{2\pi} \frac{\partial(hu^2)}{h\partial\theta} \cos\theta \, \mathrm{d}\theta$$

$$
\begin{aligned}
&= 2R^2(((\dot{X})^2 - (\dot{Y})^2)G_2^{12} + 2\dot{X}\dot{Y}G_2^{21}) \\
&\quad + 2R^2(-\dot{X}\dot{Y}G_2^{01} + C(\dot{X}G_2^{02} + \dot{Y}G_2^{11})) \\
&\quad - R^2((\dot{X})^2 X G_3^{31} + X(\dot{Y})^2 G_3^{13} - 2X\dot{X}\dot{Y}G_3^{22}) \\
&\quad - R^2(C^2 X G_3^{11} + 2CX(\dot{X}G_3^{21} - \dot{Y}G_3^{12})) \\
&\quad - R^2(-(\dot{X})^2 Y G_3^{22} - Y(\dot{Y})^2 G_3^{04} + 2Y\dot{X}\dot{Y}G_3^{13}) \\
&\quad - R^2(-C^2 Y G_3^{02} - 2CY(\dot{X}G_3^{12} - \dot{Y}G_3^{03})),
\end{aligned} \tag{A5}
$$

$$
\begin{aligned}
\mathbb{I}_3^Y(t) &\equiv \int_0^{2\pi} \frac{(\tau_s + \tau_r)}{h} \cos\theta \, \mathrm{d}\theta \\
&= \rho f \Omega R^2 (\dot{X} G_2^{11} - \dot{Y} G_2^{02} + C G_2^{01}) \\
&\quad - \frac{1}{2} \rho f \Omega^2 R^2 G_1^{01};
\end{aligned} \tag{A6}
$$

$$
\mathbb{I}_1(t) \equiv \int_0^{2\pi} \frac{\partial(hu)}{h\partial t} \, \mathrm{d}\theta = R(\ddot{X} G_1^{10} - \ddot{Y} G_1^{01} + \dot{C} G_1^{00}), \tag{A7}
$$

$$
\begin{aligned}
\mathbb{I}_2(t) &\equiv \int_0^{2\pi} \frac{\partial(hu^2)}{h\partial\theta} \, \mathrm{d}\theta \\
&= 2R^2(((\dot{X})^2 - (\dot{Y})^2) G_2^{11} + 2\dot{X}\dot{Y} G_2^{20}) \\
&\quad + 2R^2(-\dot{X}\dot{Y} G_2^{00} + C(\dot{X} G_2^{01} + \dot{Y} G_2^{10})) \\
&\quad - R^2((\dot{X})^2 X G_3^{30} + X(\dot{Y})^2 G_3^{12} - 2X\dot{X}\dot{Y} G_3^{21}) \\
&\quad - R^2(2CX(\dot{X} G_3^{20} - \dot{Y} G_3^{11})) \\
&\quad - R^2(-(\dot{X})^2 Y G_3^{21} - Y(\dot{Y})^2 G_3^{03} + 2Y\dot{X}\dot{Y} G_3^{12}) \\
&\quad - R^2(-2CY(\dot{X} G_3^{11} - \dot{Y} G_3^{02})),
\end{aligned} \tag{A8}
$$

$$
\mathbb{I}_3(t) \equiv \int_0^{2\pi} \frac{(\tau_s + \tau_r)}{h} \, \mathrm{d}\theta = \rho f \Omega R^2 (\dot{X} G_2^{10} - \dot{Y} G_2^{01} + C G_2^{00}) - \frac{1}{2} \rho f \Omega^2 R^2 G_1^{00}. \tag{A9}
$$

APPENDIX B: AZIMUTHAL INTEGRALS

The azimuthal integrals appearing in Appendix A are given as follows:

$$
G_1^{00} = \frac{2\pi}{\sqrt{H^2 - E^2}}, \tag{B1}
$$

$$
G_1^{01} = \begin{cases} 0 & \text{if } X = Y = 0, \\ 2\pi X \dfrac{H - \sqrt{H^2 - E^2}}{E^2 \sqrt{H^2 - E^2}} & \text{otherwise,} \end{cases} \tag{B2}
$$

$$
G_1^{10} = \begin{cases} 0 & \text{if } X = Y = 0, \\ 2\pi Y \dfrac{H - \sqrt{H^2 - E^2}}{E^2 \sqrt{H^2 - E^2}} & \text{otherwise,} \end{cases} \tag{B3}
$$

$$G_1^{11} = \begin{cases} 0 & \text{if } X = Y = 0, \\ -2\pi YX \dfrac{E^2 - 2H(H - \sqrt{H^2 - E^2})}{E^4\sqrt{H^2 - E^2}} & \text{otherwise} \end{cases} \tag{B4}$$

$$G_1^{20} = \begin{cases} \dfrac{\pi}{H} & \text{if } X = Y = 0, \\ 2\pi \dfrac{X^2E^2 - H(X^2 - Y^2)(H - \sqrt{H^2 - E^2})}{E^4\sqrt{H^2 - E^2}} & \text{otherwise} \end{cases} \tag{B5}$$

$$G_1^{02} = G_1^{00} - G_1^{20}$$

$$\begin{cases} \dfrac{\pi}{H} & \text{if } X = Y = 0, \\ 2\pi \dfrac{Y^2E^2 + H(X^2 - Y^2)(H - \sqrt{H^2 - E^2})}{E^4\sqrt{H^2 - E^2}} & \text{otherwise,} \end{cases} \tag{B6}$$

$$G_2^{00} = 2\pi H \frac{\sqrt{H^2 - E^2}}{(H^2 - E^2)^2}, \quad G_2^{01} = 2\pi X \frac{\sqrt{H^2 - E^2}}{(H^2 - E^2)^2}, \quad G_2^{10} = 2\pi Y \frac{\sqrt{H^2 - E^2}}{(H^2 - E^2)^2}, \tag{B7, B8, B9}$$

$$G_2^{20} = \begin{cases} \dfrac{\pi}{H^2} & \text{if } X = Y = 0, \\ 2\pi \dfrac{HY^2E^2 + (H^2(X^2 - Y^2) - X^4 + Y^4)(H - \sqrt{H^2 - E^2})}{E^4(\sqrt{H^2 - E^2})^3} & \text{otherwise,} \end{cases} \tag{B10}$$

$$G_2^{02} = G_2^{00} - G_2^{20},$$

$$G_2^{11} = \begin{cases} 0 & \text{if } X = Y = 0, \\ 2\pi XY \dfrac{H(3E^2 - 2H^2) + 2(H^2 - E^2)\sqrt{H^2 - E^2}}{E^4(\sqrt{H^2 - E^2})^3} & \text{otherwise,} \end{cases} \tag{B11}$$

$$G_2^{30} = 2\pi Y \frac{-2HY^2 + 3(H^2 - X^2)(H + \sqrt{H^2 - E^2})}{(\sqrt{H^2 - E^2})^3(H + \sqrt{H^2 - E^2})^3}, \tag{B12}$$

$$G_2^{03} = 2\pi X \frac{-2HX^2 + 3(H^2 - Y^2)(H + \sqrt{H^2 - E^2})}{(\sqrt{H^2 - E^2})^3(H + \sqrt{H^2 - E^2})^3}, \tag{B13}$$

$$G_2^{12} = G_2^{10} - G_2^{30}, \quad G_2^{21} = G_2^{01} - G_2^{03}, \tag{B14, B15}$$

$$G_3^{00} = \pi \frac{2H^2 + E^2}{(\sqrt{H^2 - E^2})^5}, \quad G_3^{20} = \pi \frac{H^2 - X^2 + 2Y^2}{(\sqrt{H^2 - E^2})^5}, \tag{B16, B17}$$

$$G_3^{02} = G_3^{00} - G_3^{20}, \quad G_3^{11} = \pi \frac{3XY}{(\sqrt{H^2 - E^2})^5}, \tag{B18, B19}$$

$$G_3^{10} = 3\pi \frac{HY}{(\sqrt{H^2 - E^2})^5}, \quad G_3^{01} = 3\pi \frac{HX}{(\sqrt{H^2 - E^2})^5}, \tag{B20, B21}$$

$$G_3^{30} = \pi Y \frac{9H^4 - 15H^2X^2 - 2Y^4 + 6X^4 + (H^2 - X^2)(9H\sqrt{H^2 - E^2} - 4Y^2)}{(\sqrt{H^2 - E^2})^5(H + \sqrt{H^2 - E^2})^3}, \quad \text{(B22)}$$

$$G_3^{03} = \pi X \frac{9H^4 - 15H^2Y^2 - 2X^4 + 6Y^4 + (H^2 - Y^2)(9H\sqrt{H^2 - E^2} - 4X^2)}{(\sqrt{H^2 - E^2})^5(H + \sqrt{H^2 - E^2})^3}, \quad \text{(B23)}$$

$$G_3^{12} = G_3^{10} - G_3^{30}, \quad G_3^{21} = G_3^{01} - G_3^{03}, \quad \text{(B24, B25)}$$

$$G_3^{40} = 3\pi \frac{(H^2 - X^2)(X^4 - 3X^2(H^2 + Y^2) + 2H^4 + 3H^2Y^2 - 4Y^4)}{(\sqrt{H^2 - E^2})^5(H + \sqrt{H^2 - E^2})^4} + 3\pi \frac{2H((H^2 - X^2 + Y^2)^2 - 2Y^2)}{(H^2 - E^2)^2(H + \sqrt{H^2 - E^2})^4}. \quad \text{(B26)}$$

$$G_3^{04} = G_3^{00} - 2G_3^{20} + G_3^{40}, \quad \text{(B27)}$$

$$G_3^{22} = G_3^{20} - G_3^{40}, \quad G_3^{13} = G_3^{11} - G_3^{31} \quad \text{(B28, B29)}$$

$$G_3^{31} = 3\pi XY \frac{(4H^2 - Y^2 - 3X^2)(H^2 - X^2) - 2Y^4}{(H + \sqrt{H^2 - E^2})^4(\sqrt{H^2 - E^2})^5} + 3\pi XY \frac{4H(H^2 - X^2)}{(H + \sqrt{H^2 - E^2})^4(H^2 - E^2)^2}. \quad \text{(B30)}$$

APPENDIX C: NOMENCLATURE

$C(t)$	integration constant
C_{st}	structural damping
E	actual rotor eccentricity: $\sqrt{X^2 + Y^2}$
E_0	static rotor eccentricity: $\sqrt{X_0^2 + Y_0^2}$
f, f_r, f_s	friction coefficients
f_{st}	structural frequency
F_X, F_Y	nonlinear fluidelastic forces
F_X^{ext}, F_Y^{ext}	external forces
$h(\theta, t)$	local gap
H	average annular gap
K_{st}	structural stiffness
L	rotor length
M_{st}	structural mass
$p(\theta, t)$	gap-averaged pressure
R	rotor radius
t	time
$u(\theta, t)$	tangential flow velocity
$X(t), Y(t)$	rotor motions
δ	reduced gap, H/R
ε	reduced static eccentricity, E_0/H
θ	azimuthal angle
λ_n	eigenvalue of the flow–structure system
ν	kinematic viscosity of the fluid
ν_n	imaginary part of the eigenvalue λ_n
ρ	fluid density
σ	variance
σ_n	real part of the eigenvalue λ_n
τ_r, τ_s	shear stresses at the rotor and stator walls
ω_n	circular frequency
Ω	spinning velocity